Planck intermediate results. XXXI. Microwave survey of Galactic supernova remnants

Planck Collaboration: M. Arnaud[66], M. Ashdown[62,5], F. Atrio-Barandela[17], J. Aumont[53], C. Baccigalupi[81], A. J. Banday[87,10], R. B. Barreiro[58], E. Battaner[89,90], K. Benabed[54,86], A. Benoit-Lévy[22,54,86], J.-P. Bernard[87,10], M. Bersanelli[30,46], P. Bielewicz[76,10,81], J. Bobin[66], J. R. Bond[9], J. Borrill[13,84], F. R. Bouchet[54,83], C. L. Brogan[74], C. Burigana[45,28,47], J.-F. Cardoso[67,1,54], A. Catalano[68,65], A. Chamballu[66,14,53], H. C. Chiang[25,6], P. R. Christensen[77,33], S. Colombi[54,86], L. P. L. Colombo[21,60], B. P. Crill[60,11], A. Curto[58,5,62], F. Cuttaia[45], R. D. Davies[61], R. J. Davis[61], P. de Bernardis[29], A. de Rosa[45], G. de Zotti[42,81], J. Delabrouille[1], F.-X. Désert[50], C. Dickinson[61], J. M. Diego[58], S. Donzelli[46], O. Doré[60,11], X. Dupac[36], T. A. Enßlin[72], H. K. Eriksen[57], F. Finelli[45,47], O. Forni[87,10], M. Frailis[44], A. A. Fraisse[25], E. Franceschi[45], S. Galeotta[44], K. Ganga[1], M. Giard[87,10], Y. Giraud-Héraud[1], J. González-Nuevo[18,58], K. M. Górski[60,91], A. Gregorio[31,44,49], A. Gruppuso[45], F. K. Hansen[57], D. L. Harrison[56,62], C. Hernández-Monteagudo[12,72], D. Herranz[58], S. R. Hildebrandt[60,11], M. Hobson[5], W. A. Holmes[60], K. M. Huffenberger[23], A. H. Jaffe[51], T. R. Jaffe[87,10], E. Keihänen[24], R. Keskitalo[13], T. S. Kisner[70], R. Kneissl[35,7], J. Knoche[72], M. Kunz[16,53,3], H. Kurki-Suonio[24,40], A. Lähteenmäki[2,40], J.-M. Lamarre[65], A. Lasenby[5,62], C. R. Lawrence[60], R. Leonardi[8], M. Liguori[27,59], P. B. Lilje[57], M. Linden-Vørnle[15], M. López-Caniego[36,58], P. M. Lubin[26], D. Maino[30,46], M. Maris[44], D. J. Marshall[66], P. G. Martin[9], E. Martínez-González[58], S. Masi[29], S. Matarrese[27,59,39], P. Mazzotta[32], A. Melchiorri[29,48], L. Mendes[36], A. Mennella[30,46], M. Migliaccio[56,62], M.-A. Miville-Deschênes[53,9], A. Moneti[54], L. Montier[87,10], G. Morgante[45], D. Mortlock[51], D. Munshi[82], J. A. Murphy[75], P. Naselsky[78,34], F. Nati[25], F. Noviello[61], D. Novikov[71], I. Novikov[77,71], N. Oppermann[9], C. A. Oxborrow[15], L. Pagano[29,48], F. Pajot[53], R. Paladini[52], F. Pasian[44], M. Peel[61], O. Perdereau[64], F. Perrotta[81], F. Piacentini[29], M. Piat[1], D. Pietrobon[60], S. Plaszczynski[64], E. Pointecouteau[87,10], G. Polenta[4,43], L. Popa[55], G. W. Pratt[66], J.-L. Puget[53], J. P. Rachen[19,72], W. T. Reach[88★], W. Reich[73], M. Reinecke[72], M. Remazeilles[61,53,1], C. Renault[68], J. Rho[80], S. Ricciardi[45], T. Riller[72], I. Ristorcelli[87,10], G. Rocha[60,11], C. Rosset[1], G. Roudier[1,65,60], B. Rusholme[52], M. Sandri[45], G. Savini[79], D. Scott[20], V. Stolyarov[5,85,63], D. Sutton[56,62], A.-S. Suur-Uski[24,40], J.-F. Sygnet[54], J. A. Tauber[37], L. Terenzi[38,45], L. Toffolatti[18,58,45], M. Tomasi[30,46], M. Tristram[64], M. Tucci[16], G. Umana[41], L. Valenziano[45], J. Valiviita[24,40], B. Van Tent[69], P. Vielva[58], F. Villa[45], L. A. Wade[60], D. Yvon[14], A. Zacchei[44], and A. Zonca[26]

(Affiliations can be found after the references)

Received ; accepted

ABSTRACT

The all-sky *Planck* survey in 9 frequency bands was used to search for emission from all 274 known Galactic supernova remnants. Of these, 16 were detected in at least two *Planck* frequencies. The radio-through-microwave spectral energy distributions were compiled to determine the emission mechanism for microwave emission. In only one case, IC 443, is there high-frequency emission clearly from dust associated with the supernova remnant. In all cases, the low-frequency emission is from synchrotron radiation. As predicted for a population of relativistic particles with energy distribution that extends continuously to high energies, a single power law is evident for many sources, including the Crab and PKS 1209-51/52. A decrease in flux density relative to the extrapolation of radio emission is evident in several sources. Their spectral energy distributions can be approximated as broken power laws, $S_\nu \propto \nu^{-\alpha}$, with the spectral index, α, increasing by 0.5–1 above a break frequency in the range 10–60 GHz. The break could be due to synchrotron losses.

Key words. ISM: Supernova remnants, Radio Continuum: ISM, Supernova Remnants: Individual: G21.5-0.9, W 44, CTB 80, Cygnus Loop, HB 21, Cas A, Tycho, 3C 58, Crab, IC 443, Puppis A, Vela, PKS 2109-51/52, RCW 86, MSH 15-5*6*, SN 1006

1. Introduction

Supernovae leave behind remnants that take on several forms (McCray & Wang 1996). The core of the star that explodes is either flung out with the rest of the ejecta into the surrounding medium (in the case of a Type I supernova), or it survives as a neutron star or black hole (in the case of a Type II supernova). The neutron stars eject relativistic particles from jets, making them visible as pulsars and powering wind nebulae. These wind nebulae are sometimes called 'plerions', and are exemplified by the Crab Nebula.

Ejecta from the stellar explosion are only visible for young ($\sim 10^3$ yr) supernova remnants, before they are mixed with surrounding interstellar or residual circumstellar material; such objects are exemplified by the historical Tycho and Kepler supernova remnants and Cassiopeia A. Type I supernovae from white dwarf deflagration leave behind supernova remnants, because their blast waves propagate into the interstellar medium. Most supernova remnants are from older explosions, and the material being observed is interstellar (and circumstellar in some cases) material shocked by the supernova blast waves. The magnetic field of the medium is enhanced in the compressed post-shock gas, and charged particles are accelerated to relativistic speeds, gen-

---

erating copious synchrotron emission that is the hallmark of a supernova remnant at radio frequencies.

At the highest radio frequencies and in the microwave, supernova remnants may transition from synchrotron emission to other mechanisms. The synchrotron brightness decreases as frequencies increase, and free-free emission (with its flatter spectrum) and dust emission (with its steeply rising spectrum) will gain prominence. Dipole radiation from spinning dust grains could possibly contribute (Scaife et al. 2007). Because the synchrotron radiation itself is an energy loss mechanism, the electrons decrease in energy over time, and relatively fewer higher-energy electrons should exist as the remnants age; therefore, the synchrotron emission will diminish at higher frequencies. For these reasons, a survey of supernova remnants at microwave frequencies could reveal some keys to the evolution of relativistic particles as they are produced and injected into the interstellar medium, as well as potentially unveiling new emission mechanisms that can trace the nature of the older supernova remnants.

2. Observations

2.1. Properties of the Planck survey

Planck[1] (Tauber et al. 2010; Planck Collaboration I 2011) is the third generation space mission to measure the anisotropy of the cosmic microwave background (CMB). It observed the sky in nine frequency bands covering 30–857 GHz with high sensitivity and angular resolution from $31'$ to $5'$. The Low Frequency Instrument (LFI; Mandolesi et al. 2010; Bersanelli et al. 2010; Mennella et al. 2011) covers the 30, 44, and 70 GHz bands with amplifiers cooled to 20 K. The High Frequency Instrument (HFI; Lamarre et al. 2010; Planck HFI Core Team 2011a) covers the 100, 143, 217, 353, 545, and 857 GHz bands with bolometers cooled to 0.1 K. A combination of radiative cooling and three mechanical coolers produces the temperatures needed for the detectors and optics (Planck Collaboration II 2011). Two data processing centres (DPCs) check and calibrate the data and make maps of the sky (Planck HFI Core Team 2011b; Zacchei et al. 2011; Planck Collaboration V 2014; Planck Collaboration VIII 2014). *Planck*'s sensitivity, angular resolution, and frequency coverage make it a powerful instrument for Galactic and extragalactic astrophysics as well as cosmology. Early astrophysics results are given in Planck Collaboration VIII–XXVI 2011, based on data taken between 13 August 2009 and 7 June 2010. Intermediate astrophysics results are being presented in a series of papers based on data taken between 13 August 2009 and 27 November 2010.

Relevant properties of *Planck* are summarized for each frequency band in Table 1. The effective beam shapes vary across the sky and with data selection. Details are given in Planck Collaboration IV (2014) and Planck Collaboration VII (2014). Average beam sizes are given in Table 1.

Table 1. Planck survey properties

Band	Center Frequency [GHz]	Beam FWHM[a] [arcmin]	Calibration Accuracy[b] [%]	Units Factor[c] [Jy pix^{-1}]
30	28.5	32.3	0.25	27.00
44	44.1	27.1	0.25	56.56
70	70.3	13.3	0.25	128.4
100	100	9.66	0.6	59.72
143	143	7.27	0.5	95.09
217	217	5.01	0.7	121.2
353	353	4.86	2.5	74.63
545	545	4.84	5	0.250
857	857	4.63	5	0.250

[a] Beams are from (Planck Collaboration VII 2014) for HFI and (Planck Collaboration IV 2014) for LFI

[b] Calibration is from (Planck Collaboration VIII 2014) for HFI and (Planck Collaboration V 2014) for LFI

[c] Pixel sizes refer to the all-sky Healpix maps and are $11.8'$ for frequencies 30–70 GHz and $2.9'$ for frequencies 100-857 GHz.

Calibration of the brightness scale was achieved by measuring the amplitude of the dipole of the cosmic microwave background (CMB) radiation, which has a known spatial and spectral form; this calibration was used for the seven lower frequency bands (30–353 GHz). At the two high frequencies (545 and 857 GHz), the CMB signal is relatively low, so calibration was performed using measurements of Uranus and Neptune. The accuracy of the calibration is given in Table 1; the *Planck* calibration is precise enough that it is not an issue for the results discussed in this paper.

The *Planck* image products are at Healpix (Górski et al. 2005) $N_{\rm side} = 2048$ for frequencies 100–857 GHz and $N_{\rm side} = 1024$ for frequencies 30–70 GHz, in units of CMB thermodynamic temperature up to 353 GHz. For astronomical use, the temperature units are converted to flux density per pixel by multiplication by the factor given in the last column of Table 1. At 545 and 857 GHz, the maps are provided in MJy sr^{-1} units, and the scaling simply reflects the pixel size.

2.2. Flux density measurements

Flux densities were measured using circular aperture photometry. Other approaches to measuring the source fluxes were explored and could be pursued by future investigators. This includes model fitting (e.g. Gaussian or other source shape motivated by morphology seen at other wavelengths convolved with the beam) or non-circular aperture photometry (e.g. drawing a shape around the source and hand-selecting a background). We experimented with both methods and found they were highly dependent upon the choices made. The circular-aperture method used in this paper has the advantages of being symmetric about the source center (hence, eliminating all linear gradients in the background) as well as being objective about the shape of the source (hence, independent of assumptions about the microwave emitting region).

Because of the wide range of *Planck* beam sizes and the comparable size of the supernova remnants (SNRs), we took care to adjust the aperture sizes as a function of frequency and to scale the results to a flux density scale. For each SNR, the source size in the maps was taken to be the

combination of the intrinsic source size from the Green catalogue (Green 2009), θ_{SNR} in Table 2, and the *Planck* beam size, θ_{b} in Table 1:

$$\theta_{\mathrm{s}} = \sqrt{\theta_{\mathrm{SNR}}^2 + \theta_{\mathrm{b}}^2}. \tag{1}$$

The flux densities were measured using standard aperture photometry, with the aperture size centred on each target with a diameter scaled to $\theta_{\mathrm{ap}} = 1.5\theta_{\mathrm{s}}$. The background was determined in an annulus of inner and outer radii $1.5\theta_{\mathrm{ap}}$ and $2\theta_{ap}$. To correct for loss of flux density outside of the aperture, an aperture correction as predicted for a Gaussian flux density distribution with size θ_s was applied to each measurement:

$$f_{\mathrm{A}} = \frac{1}{f(\theta_{\mathrm{ap}}) - [f(\theta_{\mathrm{out}}) - f(\theta_{\mathrm{in}})]} \tag{2}$$

where the flux density enclosed within a given aperture is

$$f(\theta) = 1 - e^{-4\ln 2(\theta/\theta_{\mathrm{s}})^2} \tag{3}$$

and θ_{in} and θ_{out} are the inner and outer radii of annulus within which the background is measured. For the well-resolved sources (diameter 50 % larger than the beam FWHM), no aperture correction was applied. Aperture corrections are typically 1.5 for the compact sources and by definition unity for the large sources. The use of a Gaussian source model for the intermediate cases (source comparable to beam) is not strictly appropriate for SNRs, which are often limb-brightened (shell-like), so the aperture corrections are only good to about 20 %.

The uncertainties for the flux densities are a root-sum-square of the calibration uncertainty (from Table 1) and the propagated statistical uncertainties. The statistical uncertainties (technically, appropriate for white uncorrelated noise only) take into account the number of pixels in the on-source aperture and background annulus and using the robust standard deviation within the background annulus to estimate the pixel-to-pixel noise for each source. The measurements are made using the native `Healpix` maps, by searching for pixels within the appropriate apertures and background annuli and calculating the sums and robust medians, respectively. This procedure avoids the need of generating extra projections and maintains the native pixelization of the survey.

We verify the flux calibration scale by using the procedure described above on the well-measured Crab Nebula. The flux densities are compared to previous measurements in Fig. 1. The good agreement verifies the measurement procedure used for this survey, at least for a compact source. The *Planck* Early Release Compact Source Catalogue (Planck Collaboration VII 2011, hereafter ERCSC) flux density measurements for the Crab are lower than those determined in this paper, due to the source being marginally resolved by *Planck* at high frequencies.

Table 2 lists the basic properties of SNRs that were detected by *Planck*. Table 3 summarises the *Planck* flux-density measurements for detected SNRs. To be considered a detection, each SNR must have a statistically significant flux density measurement (flux density greater than 3.5 times the statistical uncertainty in the aperture photometry measurement) and be evident by eye for at least two *Planck* frequencies. Inspection of the higher-frequency images allows for identification of interstellar foregrounds for
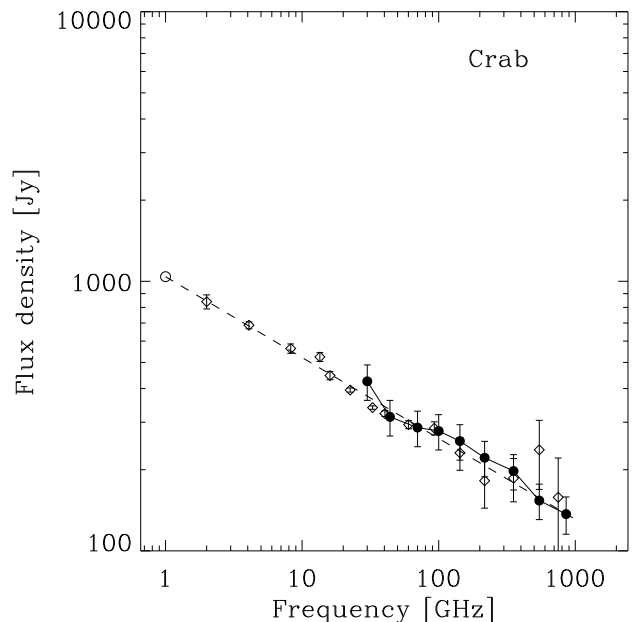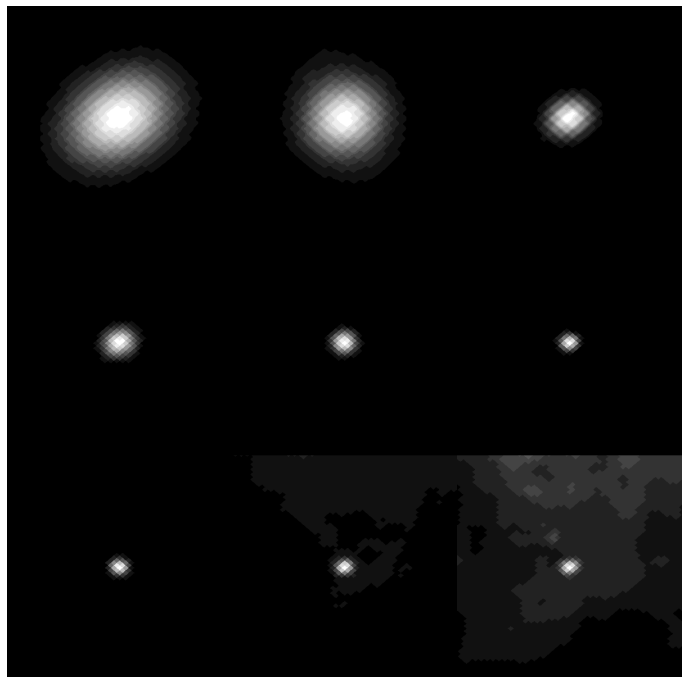

Fig. 1. *Top*: *Planck* Images of the Crab nebula at frequencies increasing from 30 GHz at top left to 857 GHz at bottom right. Each image is $100'$ on a side, with the three lowest-frequency images smoothed by $7'$. *Bottom*: Microwave spectral energy distribution of the Crab Nebula. Filled circles are *Planck* measurements with 3σ error bars. The open symbol at 1 GHz and the dashed line emanating from it are the flux and power law with spectral index from the Green catalogue. Open diamonds are from the compilation of flux densities by Macías-Pérez et al. (2010).

the supernova remnants, which are almost all best-detected at the lowest frequencies. A large fraction of the SNRs are located close to the Galactic plane and are smaller than the low-frequency *Planck* beam. Essentially none of those targets could be detected with *Planck* due to con-

fusion from surrounding H II regions. Dust and free-free emission from H II regions makes them extremely bright at far-infrared wavelengths and moderately bright at radio frequencies. Supernova remnants in the Galactic plane would only be separable from H II regions using a multi-frequency approach and angular resolution significantly higher than *Planck*. More detailed results from the flux measurements are provided in the Appendix.

As a test of the quality of the results and robustness to contamination from the CMB, we performed the flux density measurements using the total intensity maps as well as the CMB-subtracted maps. Differences greater than 1σ were seen only for the largest SNRs. Of the measurements in Table 3, only the following flux densities were affected at the 2-σ or greater level: Cygnus Loop (44 and 70 GHz), HB 21 (70 GHz), and Vela (70 GHz).

3. Results and discussion of individual objects

The images and spectral energy distributions (SEDs) of detected SNRs are summarized in the following subsections. A goal of the survey is to determine whether new emission mechanisms or changes in the radio emission mechanisms are detected in the microwave range. Therefore, for each target, the 1 GHz radio flux density (Green 2009) was used to extrapolate to microwave frequencies using a power law. The extrapolation illustrates the expected *Planck* flux densities, if synchrotron radiation is the sole source of emission and the high-energy particles have a power-law energy distribution. The Green (2009) SNR catalogue was compiled from an extensive and continuously updated literature search. The radio spectral indices are gleaned from that same compendium. They represent a fit to the flux densities from 0.4 to 5 GHz, where available, and are the value α in a SED $S_\nu = S_\nu(1\,\mathrm{GHz})\nu_{\mathrm{GHz}}^{-\alpha}$. The spectral indices can be quite uncertain in some cases, where observations with very different observing techniques are combined (in particular, interferometric and single-dish). The typical spectral index for synchrotron emission from SNRs is $\alpha \sim 0.4 - 0.8$. On theoretical grounds (Reynolds 2011), it has been shown that for a shock that compresses the gas by a factor r, the spectral index of the synchrotron emission from the relativistic electrons in the compressed magnetic field has index $\alpha = 3/(2r-2)$. For a strong adiabatic shock, $r = 4$, so the expected spectral index is $\alpha = 0.5$, similar to the typical observed value for SNRs. Shallower spectra are seen towards pulsar wind nebulae, where the relativistic particles are freshly injected.

Where there was a positive deviation relative to the radio power law, there would be an indication of a different emission mechanism. Free-free emission has a radio spectral index $\alpha \sim 0.1$ that is only weakly dependent upon the electron temperature. Ionized gas near massive star-forming regions dominates the microwave emission from the Galactic plane and is a primary source of confusion for the survey presented here. Small SNRs in the Galactic plane are essentially impossible to detect with *Planck* due to this confusion. Larger SNRs can still be identified because their morphology can be recognized by comparison to lower-frequency radio images.

At higher *Planck* frequencies, thermal emission from dust grains dominates the sky brightness. The thermal dust emission can be produced in massive star forming regions (just like the free-free emission), as well as in lower-mass

star forming regions, where cold dust in molecular clouds contributes. Confusion due to interstellar dust makes identification of SNRs at the higher *Planck* frequencies essentially impossible without a detailed study of individual cases, and even then the results will require confirmation. For the present survey we only measure four SNRs at frequencies 353 GHz and higher; in all cases the targets are bright and compact, making them distinguishable from unrelated emission.

3.1. G21.5-0.9

G21.5-0.9 is a supernova remnant and pulsar wind nebula, powered by the recently-discovered PSR J1833-1034 (Gupta et al. 2005; Camilo et al. 2006), with an estimated age less than 870 yr based on the present expansion rate of the supernova shock (Bietenholz & Bartel 2008). The *Planck* images in the upper panels of Figure 2 show the SNR as a compact source at intermediate frequencies. The source is lost in confusion with unrelated galactic plane structures at 30–44 GHz and at 217 GHz and higher frequencies. In addition to the aperture photometry as performed for all targets, we made a Gaussian fit at 70 GHz to the source to ensure the flux refers to the compact source and not diffuse emission. The fitted Gaussian had a lower flux (2.7 Jy) than aperture photometry (4.3 Jy), but the residual from the Gaussian fit still shows the source and is clearly an underestimate. Fitting with a more complicated functional form would yield a somewhat higher flux, so we are confident in the aperture photometry flux we report in Table 3.

The lower panel of Figure 2 shows the *Planck* flux densities together with radio data. The SED is relatively flat, more typical of a pulsar wind nebula than synchrotron emission from an old SNR shock. The microwave SED has been measured at two frequencies, and the *Planck* flux densities are in general agreement. A single power law cannot fit the observations, as has been noted by Salter et al. (1989). Instead, we show in Fig. 2 a broken power law, which would be expected for a pulsar wind nebula, with a change in spectral index by +0.5 above a break frequency (Reynolds 2009). The data are consistent with a break frequency at 40 GHz and a relatively flat, $\alpha = 0.05$ spectral index at lower frequencies.

3.2. W 44

W 44 is one of the brightest radio SNRs but is challenging for *Planck* because of its location in a very crowded portion of the Galactic plane. Figure 3 shows the *Planck* images and flux densities. The synchrotron emission is detected above the unrelated nearby regions at 30–70 GHz. Above 100 GHz, there is a prominent structure in the *Planck* images that is at the western (left-hand side in Fig. 3) border of the radio SNR but has a completely different morphology; we recognise this structure as being a compact H II region in the radio images, unrelated to the W 44 SNR even if possibly due to a member of the same OB association as the progenitor. At 70 GHz, the H II region flux is 22 Jy, comparable to the SNR; we ensured that there is no contamination of the SNR flux by slightly adjusting the aperture radius to exclude the H II region. The *Planck* 70 GHz flux density is somewhat lower than the radio power law, while the 30 GHz flux den-

Table 2. Properties of detected supernova remnants.

Supernova remnant		Angular [a] Diameter ($'$)	$S_{1\,\mathrm{GHz}}$ [a] (Jy)	Spectral[a] Index	Notes[b]
G21.5-0.9	G21.5-0.9	4	7	0.00	$< 10^3$ yr, pulsar
G34.7-0.4	W 44	35	230	0.37	2×10^4 yr, dense
G69.0+2.7	CTB 80	80	120	. . .	10^5 yr, pulsar, plerion
G74.0-8.5	Cygnus Loop	230	210	. . .	mature
G89.0+4.7	HB 21	120	220	0.38	5000 yr, dense
G111.7-2.1	Cas A	5	2720	0.77	330 yr, ejecta, CCO
G120.1+1.4	Tycho	8	56	0.65	young, Type Ia
G130.7+3.1	3C 58	9	33	0.07	830 yr, plerion, pulsar
G184.6-5.8	Crab	7	1040	0.30	958 yr, plerion, pulsar
G189.1+3.0	IC 443	40	160	0.36	3×10^4 yr, dense ISM, CCO
G260.4-3.4	Puppis A	60	130	0.50	CCO, 3700 yr
G263.9-3.3	Vela	255	1750	. . .	10^4 yr
G296.5+10.0	PKS 1209-51/52	90	48	0.5	$\sim 10^4$ yr
G315.4-2.3	RCW 86	42	49	0.60	1800 yr
G326.3-1.8	MSH 15-5$6$	38	145	. . .	
G327.6+14.6	SN 1006	30	19	0.60	1008 yr, Type Ia

[a] Flux densities at 1 GHz, radio spectral indices, and angular diameters are from Green (2009). For cases of unknown or strongly-spatially-variable spectral index, we put '. . .' in the table and use a nominal value of 0.5 in the figures for illustration purposes only.

[b] Notes on the properties of the SNR, gleaned from the Green (2009) catalogue and references therein, as well as updates from the online version http://www.mrao.cam.ac.uk/projects/surveys/snrs/. *Plerion*: radio emission is centre-filled. *Pulsar*: a pulsar is associated with the SNR. *CCO*: a central compact object (presumably a neutron star) is associated with the supernova remnant from high-energy images. *Dense ISM*: the supernova remnant is interacting with a dense interstellar medium. *X* yr: estimated age of the supernova remnant. *Mature*: age likely greater than 10^5 yr. *Type X*: the supernova that produced this supernova remnant was of type *X*.

Table 3. *Planck* integrated flux density measurements of supernova remnants.

Source	Flux density [Jy]								
	30 GHz	44 GHz	70 GHz	100 GHz	143 GHz	217 GHz	353 GHz	545 GHz	857 GHz
G21.5-0.9	. . .	. . .	4.3 $\pm$ 0.6	2.7 $\pm$ 0.5	3.0 $\pm$ 0.4	. . .	. . .	. . .	. . .
W 44	121 $\pm$ 8	68 $\pm$ 5	30 $\pm$ 5	. . .	. . .	. . .	. . .	. . .	. . .
CTB 80	12.2 $\pm$ 1.7	3.7 $\pm$ 1.2	. . .	. . .	. . .	. . .	. . .	. . .	. . .
Cygnus Loop .	24.9 $\pm$ 1.7	. . .	. . .	. . .	. . .	. . .	. . .	. . .	. . .
HB 21	14.7 $\pm$ 1.7	11.9 $\pm$ 1.3	. . .	. . .	. . .	. . .	. . .	. . .	. . .
Cas A	228 $\pm$ 11	140 $\pm$ 7	109 $\pm$ 6	94 $\pm$ 5	73 $\pm$ 4	62 $\pm$ 4	52 $\pm$ 7	. . .	. . .
Tycho	8.1 $\pm$ 0.4	5.2 $\pm$ 0.3	4.4 $\pm$ 0.3	4.0 $\pm$ 0.2	3.5 $\pm$ 0.2	. . .	. . .	. . .	. . .
3C 58	22.2 $\pm$ 2.2	16.4 $\pm$ 1.6	14.2 $\pm$ 1.4	12.7 $\pm$ 1.3	10.8 $\pm$ 1.1	8.4 $\pm$ 0.8	4.8 $\pm$ 0.7	. . .	. . .
Crab	425 $\pm$ 21	314 $\pm$ 16	287 $\pm$ 14	278 $\pm$ 14	255 $\pm$ 13	222 $\pm$ 11	198 $\pm$ 10	154 $\pm$ 7.7	137 $\pm$ 7
IC 443	56 $\pm$ 3	39 $\pm$ 3	20.5 $\pm$ 1.2	17.3 $\pm$ 0.9	11.1 $\pm$ 0.8	56 $\pm$ 10	229 $\pm$ 30	720 $\pm$ 100	2004 $\pm$ 300
Puppis A	32.0 $\pm$ 1.7	21.9 $\pm$ 1.2	13.6 $\pm$ 1.1	4.5 $\pm$ 0.8	. . .	. . .	. . .	. . .	. . .
Vela	488 $\pm$ 25	345 $\pm$ 17	289 $\pm$ 15	. . .	. . .	. . .	. . .	. . .	. . .
PKS 1209	9.3 $\pm$ 0.5	7.0 $\pm$ 0.6	5.5 $\pm$ 1.1	4.0 $\pm$ 0.4	. . .	. . .	. . .	. . .	. . .
RCW 86	3.7 $\pm$ 1.0	4.8 $\pm$ 0.7	3.3 $\pm$ 0.6	. . .	. . .	. . .	. . .	. . .	. . .
MSH 15-5$6$ . . .	56 $\pm$ 4	39 $\pm$ 3	22.4 $\pm$ 1.5	20.6 $\pm$ 1.7	12.8 $\pm$ 2.7 . . .	. . .	. . .	. . .	. . .
SN1006	3.2 $\pm$ 0.2	2.2 $\pm$ 0.3	1.0 $\pm$ 0.3	0.7 $\pm$ 0.1	. . .	. . .	. . .	. . .	. . .

sity is higher. We consider the discrepancy at 30 GHz flux density as possibly due to confusion with unrelated large-scale emission from the Galactic plane. Figure 3 includes a broken power law that could explain the lower 70 GHz flux density, but the evidence from this single low flux density, especially given the severe confusion from unrelated sources in the field, does not conclusively demonstrate the existence of a spectral break for W 44.

3.3. CTB 80

CTB 80 is powered by a pulsar that has traveled so far from the centre of explosion that it is now within the shell and injecting high-energy electrons directly into the swept-up ISM. Figure 4 shows that the SNR is only clearly detected at 30 and 44 GHz, being lost in confusion with the unrelated

ISM at higher frequencies. The SNR is marginally resolved at low *Planck* frequencies, and the flux measurements include the entire region evident in radio images (Castelletti et al. 2003). The *Planck* flux densities at 30 and 44 GHz are consistent with a spectral index around $\alpha \simeq 0.8$, as shown in Fig. 4, continuing the trend that had previously been identified based on 10.2 GHz measurements (Sofue et al. 1983). The spectral index in the microwave is definitely steeper than that seen from 0.4 to 1.4 GHz, $\alpha = 0.45 \pm 0.03$ (Kothes et al. 2006), though the steepening is not as high as discussed above for pulsar wind nebulae where $\Delta\alpha = 0.5$ can be due to significant cooling from synchrotron self-losses.

3.4. Cygnus Loop

The Cygnus Loop is one of the largest SNRs on the sky, with an angular diameter of nearly 4°. To measure the flux density, we use an on-source aperture of 120′ with a background annulus from 140′ to 170′. On these large scales, the CMB fluctuations are a significant contamination, so we subtracted the CMB using the SMICA map (Planck Collaboration XII 2014). The SNR is well detected at 30 GHz by *Planck*; a similar structure is evident in the 44 and 70 GHz maps, but the total flux density could not be accurately estimated at these frequencies due to uncertainty in the CMB subtraction. The NW part of the remnant, which corresponds to NGC 6992 optically, was listed in the ERCSC as an LFI source with "no plausible match in existing radio catalogues." The actual match to the Cygnus Loop was made by AMI Consortium et al. (2012) as part of their effort to clarify the nature of such sources.

For the purpose of illustrating the complete SED, we estimated the fluxes at all *Planck* frequencies. Figure 5 shows the SED. The low-frequency emission is well matched by a power law with spectral index $\alpha = 0.46 \pm 0.02$ from 1 to 60 GHz. For comparison, a recent radio survey (Sun et al. 2006; Han et al. 2013) measured the spectral index for the synchrotron emission from the Cygnus Loop and found a synchrotron index $\alpha = 0.40 \pm 0.06$, in excellent agreement with the *Planck* results. There is no indication of a break in the power-law index all the way up to 60 GHz (where dust emission becomes important). As discussed by Han et al. (2013), previous indications of a break in the spectral index at much lower frequencies are disproved both by the 5 GHz flux density they reported and now furthermore by the 30 and 44 GHz flux densities reported here.

At high *Planck* frequencies, the images in Fig. 5 show bright structured emission toward the upper right corner (celestial E) and extending well outside the SNR; this unrelated emission is due to dust in molecular clouds illuminated by massive stars in the Cygnus-X region. The bright, unrelated emission makes the measurement of high-frequency fluxes of the Cygnus Loop problematic; the (heavily contaminated) aperture fluxes are well matched by a modified-blackbody fitted to the data with emissivity index $\beta = 1.46 \pm 0.16$ and temperature $T_d = 17.6 \pm 1.9$ K, typical of molecular clouds. The infrared emission from the SNR shell itself was detected at 60–100 μm by Arendt et al. (1992), who derived a dust temperature of 31 K. The counterpart in the *Planck* images is not evident in Fig. 5. Because the dust in the SNR shell is warmer than the ISM, we can use the 545 GHz emission as a tracer of the unrelated emission and subtract it from the 857 GHz image to locate warmer dust. The subtracted image shows faint emission that is clearly associated the shell with a surface brightness (after subtracting the scaled 545 GHz image) at 857 GHz of 0.2 MJy sr^{-1}, where the 100 μm surface brightness is 8 MJy sr^{-1}. This surface brightness ratio can be explained by a modified blackbody for dust with a temperature $T_d = 31 \pm 4$ K and an emissivity index $\simeq 1.5$, confirming the temperature measurement by Arendt et al. (1992).

3.5. HB 21

Figure 6 shows the microwave images and SED of the large SNR HB 21. The source nearly fills the displayed image and is only clearly seen at 30 and 44 GHz. A compact radio continuum source, 3C 418, appears just outside the northern boundary of the SNR and has a flux density of approximately 2 Jy at 30 and 44 GHz. The presence of this source at the boundary between the SNR and the background-subtraction annulus perturbs the flux density of the SNR by at most 1 Jy, less than the quoted uncertainty. The radio SED of HB 21 is relatively shallow, with $\alpha = 0.38$ up to 5 GHz (Fig. 6). The *Planck* flux densities at 30 and 44 GHz are significantly below the extrapolation of this power law. The target is clearly visible at both frequencies, and we confirmed that the flux densities are similar in maps with and without CMB subtraction, so the low flux density does not appear to be caused by a cold spot in the CMB.

It therefore appears that the low flux densities in the microwave are due to a spectral break. For illustration, Fig. 6 shows a model where the spectral break is at 3 GHz and the spectral index changes by $\Delta\alpha = 0.5$ above that frequency. An independent study of HB 21 found a spectral break at 5.9 ± 1.2 GHz which is reasonably consistent with our results (Pivato et al. 2013). This could occur if there have been significant energy losses since the time the high-energy particles were injected. This is probably the lowest frequency at which the break could occur and still be consistent with the radio flux densities. Even with this low value of $\nu_{\rm break}$, the *Planck* flux densities are over predicted. The spectral index change is likely to be greater than 0.5, which is possible for inhomogenous sources (Reynolds 2009). Given its detailed filamentary radio and optical morphology, HB 21 certainly fits in this category. The large size of the SNR indicates it is not young, so some significant cooling of the electron population is expected.

3.6. Cas A

Cas A is a very bright radio SNR, likely due to an historical supernova approximately 330 yr ago (Ashworth 1980). In the *Planck* images (Fig. 7), Cas A is a distinct compact source from 30–353 GHz. Cas A becomes confused with unrelated Galactic clouds at the highest *Planck* frequencies (545 and 857 GHz). Inspecting the much higher-resolution images made with *Herschel*, it is evident that at 600 GHz the cold interstellar dust would not be separable from the SNR (Barlow et al. 2010). Confusion with the bright and structured interstellar medium has made it difficult to assess the amount of material directly associated with the SNR. Figure 7 shows that from 30 to 143 GHz, the *Planck* SED closely follows an extrapolation of the radio power law. Cas A was used as a calibration verification for the *Planck* Low-Frequency Instrument, and the flux densities at 30, 44, and 70 GHz were shown to match very well the radio synchrotron power law and measurements by WMAP (Planck Collaboration V 2014).

The flux densities at 217 and 353 GHz appear higher than expected for synchrotron emission. We remeasured the excess at 353 GHz using aperture photometry with different background annuli, to check the possibility that unrelated Galactic emission is improperly subtracted and positively contaminates the flux density. At 353 GHz, the flux density could be as low as 45 Jy, which was obtained using a narrow aperture and background annulus centred on the source, or as high as 58 Jy, obtained from a wide aperture and background annulus, so we estimate a flux density and systematic uncertainty of 52 ± 7 Jy. The flux density in

the ERCSC is 35.2 ± 2.0, which falls close to the radio synchrotron extrapolation. The excess flux density measured above the synchrotron prediction is 22 ± 7, using the techniques in this paper, which is significant. This excess could potentially be due to a coincidental peak in the unrelated foreground emission or to cool dust in the SNR, which is marginally resolved by *Planck*. Images at the lowest frequency (600 GHz) observed with the *Herschel* Space Observatory (Barlow et al. 2010) at much higher angular resolution than *Planck* show that the non-synchrotron microwave emission is a combination of both cold interstellar dust and freshly formed dust.

3.7. Tycho

The Tycho SNR comprises ejecta from a supernova explosion in 1572 AD. *Planck* detects the SNR from 30 to 545 GHz and tentatively at 857 GHz, as can be seen in the images in Fig. 8. The SED shows at least two emission mechanisms. A continuation of the synchrotron spectrum dominates the 30–143 GHz flux density, while a steeply-rising contribution, most likely due to dust, dominates above 143 GHz. The SNR is well-detected by *Herschel* (Gomez et al. 2012), with its excellent spatial resolution. The *Herschel* image shows that cold dust emission is predominantly *outside* the boundary of the ejecta-dominated portion of the SNR. While some is correlated with unrelated molecular clouds, much of this emission is attributed to swept-up ISM (as opposed to ejecta). From the *Herschel* study, the dust emission was fit with a cold component at temperature 21 K. The emissivity index of the modified blackbody that fits the *Herschel* and *Planck* SED is $\beta = 1$. (The value of the emissivity index we report, $\beta = 1$, is different from the $\beta = 1.5$ described by Gomez et al. 2012 in the text of their paper, but the cold dust model plotted in their Fig. 12 appears closer to $\beta \simeq 1$, in agreement with our Fig. 8.)

3.8. 3C 58

3C 58 is a compact source at *Planck* frequencies, with a $9' \times 5'$ radio image size, so it becomes gradually resolved at frequencies above 100 GHz. The adopted aperture photometry and correction procedure in this survey should recover the entire flux density of this SNR at all frequencies. Figure 9 shows the SED. The flux density at 30 GHz is just a bit lower than that predicted by extrapolating the 1 GHz flux density with the radio spectral index. However, it is clear from the *Planck* data that the brightness declines much more rapidly than predicted by an extrapolation of the radio SED.

The *Planck* flux densities are in agreement with the low 84 GHz flux density that had been previously measured by Salter et al. (1989), who noted that their flux density measurement was 3σ below an extrapolation from lower frequencies. The *Planck* data show that the decline in flux density, relative to an extrapolation from lower frequencies, begins around or before 30 GHz and continues to at least 353 GHz.

There is a large gap in frequencies between the microwave and near-infrared detections of the pulsar wind nebula. To fill in the SED, we reprocessed the *IRAS* survey data using the HIRES algorithm (Aumann et al. 1990), and

Table 4. Flux densities for 3C 58

Frequency [GHz]	Flux [Jy]	Uncertainty [Jy]	Reference
0.151	36.0	4.0	Green (1986)
0.327	33.9	3.0	Bietenholz & Bartel (2008)
0.408	32.2	2.0	Kothes et al. (2006)
1.42	31.9	1.0	Kothes et al. (2006)
2.7	30	3	Green (1986)
15	26.7	0.5	Green et al. (1975)
30	22.2	2.2	this paper (*Planck*)
32	25.2	1.4	Morsi & Reich (1987)
44	16.4	1.6	this paper (*Planck*)
70	14.2	1.4	this paper (*Planck*)
84.2	15	2.0	Salter et al. (1989)
100	12.7	1.3	this paper (*Planck*)
143	10.8	1.1	this paper (*Planck*)
217	8.4	0.8	this paper (*Planck*)
353	4.8	0.7	this paper (*Planck*)
588	2.1	0.4	this paper (*Herschel*)
5000	0.37	0.15	this paper (*IRAS*)
66666	0.071	0.028	Slane et al. (2008)
83333	0.028	0.012	Slane et al. (2008)

we find a tentative detection of the SNR at $60\,\mu$m with a flux density of 0.4 Jy. At $100\,\mu$m the SNR is expected to be brighter, but is confused with the relatively-brighter diffuse interstellar medium. In the far-infrared, we obtained the *Herschel*/SPIRE map, created for 3C 58 as part of a large guaranteed-time key project led by M. Groenewegen, from the *Herschel* Science Archive. Figure 10 shows a colour combination of the SPIRE images. The SNR is clearly evident due to its distinct colours with respect to the diffuse ISM. In addition to the diffuse emission of the SNR, there is a compact peak in the emission at the location of the pulsar J0205+6449. We measure the flux density of the SNR to be 2.1 ± 0.4 Jy using an elliptical aperture of the same size as the radio image, and we measure the compact peak from the pulsar to be 0.05 ± 0.02 Jy using a small circular aperture centred on the pulsar with a background region surrounding the pulsar and within the SNR. Table 4 summarizes the flux densities for 3C 58 from radio through infrared frequencies. For the *Planck* fluxes, because the source is compact, a conservative uncertainty estimate of 10% is included.

3C 58 is a pulsar wind nebula, like the Crab. The shallow spectral index ($S_\nu \propto \nu^{-\alpha}$ with $\alpha = 0.07$) at low frequencies is due to injection of energetic particles into the nebula from the pulsar with an energy spectrum $dN/dE \propto E^{-s}$, with $s = 2\alpha + 1 = 1.14$. The electrons cool (become non-relativistic), which leads to a steepening of the spectrum, $\alpha \to \alpha + 0.5$ (Reynolds 2009), above a break frequency that depends upon the magnetic field and age. As an alternative to the idea of electron cooling, breaks in the synchrotron spectral index could also simply reflect breaks in the energy distribution of the relativistic particles injected into the pulsar wind nebula. Determining the location of the microwave spectral break was deemed 'crucial, as are flux measurements in the sub-mm band' (Slane et al. 2008). The present paper provides both such measurements.

The *Planck* flux densities match the electron-cooling model for a break frequency around 20 GHz. Figure 11 shows a wider-frequency version of the SED for 3C 58. The

existence of a break in the radio spectrum was previously indicated by a measurement at 84 GHz (Salter et al. 1989) that is now confirmed by the *Planck* data with six independent measurements at frequencies from 30 to 217 GHz. The *Wilkinson Microwave Anisotropy Probe* also clearly shows the decrease in flux density at microwave frequencies (Weiland et al. 2011), and the curved spectral model from their paper is at least as good a fit to the data as the broken power law. At higher frequencies, the *IRAS* and *Spitzer* measurements are significantly over-predicted by the extrapolation of the microwave SED that matches the *Planck* data. Green & Scheuer (1992) had already used the *IRAS* upper limit to show the synchrotron spectral index must steepen before reaching the far-infrared. There may be, as indicated by Slane et al. (2008), a second spectral break. We found that a good match to the radio through infrared SED can be made with a second break frequency at 200 GHz. The nature of this second break frequency is not yet understood.

3.9. IC 443

The SNR IC 443 is well known from radio to high-energy astrophysics, due to the interaction of a blast wave with both low and high-density material. The SNR is detected at all nine *Planck* frequencies. The utility of the microwave flux densities is illustrated by comparing the observations of IC 443 to extrapolations based only on lower-frequency data. In one recent paper, there is a claim for an additional emission mechanism at 10 GHz and above, with thermal free-free emission contributing at a level comparable to or higher than synchrotron radiation (Onić et al. 2012). The highest-frequency data point considered in that paper was at 8 GHz. In Fig. 12 it is evident that the proposed model including free-free emission is no better fit than a power-law scaling of the 1 GHz flux density using the spectral index from the Green catalogue. The 10.7 GHz and 30 GHz flux densities are consistent with a single power law from 1–30 GHz, with the single outlier at 8 GHz being little more than 1σ away. Both the model of Onić et al. (2012) and the single power law predict the flux density at 30 GHz perfectly, but they over predict the higher-frequency emission at 40 and 143 GHz by factors of more than 3 and 2, respectively. Therefore, the shape of the IC 443 SED requires a *dip* in emissivity in the microwave, rather than an excess due to free-free emission. The decrease in flux density could be due to a break in the synchrotron power law from the injection mechanism of the energetic particles, or due to cooling losses by the energetic particles.

At the higher *Planck* frequencies, another emission mechanism besides synchrotron radiation dominates the brightness. The horseshoe-shaped eastern portion of the SNR is evident with similar morphology at 100 GHz and higher frequencies. The southern part of the SNR, where shocks are impacting a molecular cloud (Rho et al. 2001), is physically distinct; this region becomes significantly brighter at frequencies of 217 GHz and above. While uncertainty in background subtraction makes an accurate flux difficult to measure, the fluxes were estimated all the way to 857 GHz for the purpose of Fig. 12. Based on the steep rise to higher frequency, and the similarity between the image at high and low frequencies, the higher-frequency emission is likely due to dust grains that survive the shock. Contamination by unrelated Galactic plane emission is sig-

nificant at these frequencies. Inspecting Fig. 12, it is evident that the SNR is well detected even at the highest *Planck* frequencies, because it is well resolved and its spatial pattern can be recognised in the images. To determine whether the 857 GHz flux density is due to the SNR or unrelated emission, we inspect the image along the ring of the SNR, finding an average brightness of $7 \, \mathrm{K_{cmb}}$ above the surrounding background, which is equivalent to an average surface brightness of $21 \, \mathrm{MJy \, sr^{-1}}$. The solid angle of the ring is $2\pi\theta\Delta\theta$, with $\theta = 80'$ being the radius of the SNR and $\Delta\theta \simeq 5'$ being the thickness of the ring. The total flux density from this rough estimate is 3000 Jy, which is in order-of-magnitude agreement with the flux density shown in Fig. 12. This affords some quality verification of the measured flux density of the SNR dust emission.

The shape of the SED across radio and microwave frequencies can be reasonably approximated by a combination of synchrotron and dust emission. A fit to the SED shows the dust emission has a temperature of $T = 16 \, \mathrm{K}$ with emissivity index $\beta = 1.5$, where the dust emission depends on frequency as $\nu^{-\beta}B_\nu(T)$, and $B_\nu(T)$ is the Planck function at temperature T. The precise values are not unique and require combination with infrared data and multiple temperature components given the complex mixture of dust in molecular, atomic, and shocked gas; dust dominates at frequencies above 140 GHz. The synchrotron emission follows a power law with spectral index of 0.36 from radio frequencies up to 40 GHz, after which the spectral index steepens to 1.5. The increase in spectral index is what makes IC 443 relatively faint in the range 70–143 GHz, compared to what might be expected from an extrapolation of the radio power law. Possible causes for spectral breaks are discussed for other SNRs in sections that follow.

3.10. Puppis A

The bright SNR Puppis A is evident in the *Planck* images at 30–143 GHz. The flux densities measured from the *Planck* images at 30–70 GHz roughly follow an extrapolation of the radio power law, suggesting the emission mechanism is synchrotron emission. The 100 GHz measurement is below the power law. While this measurement is challenging due to contamination from unrelated emission evident in images at higher frequencies, the flux density at 100 GHz does appear lower than the power law. A simple fit of a broken power law in Fig. 13 has a break frequency $\nu_{\mathrm{break}} = 40 \, \mathrm{GHz}$ above which the spectral index increases from 0.46 to 1.46. This fit is consistent with results from a study of WMAP observations (Hewitt et al. 2012).

3.11. Vela

The very large Vela SNR is prominent in the lowest-frequency *Planck* images; Figure 14 shows a well-resolved shell even at 30 GHz. The centre of the image is shifted (by $1°$ upward in galactic latitude) from the Green catalogue position, so as to include the entire SNR shell. The object at the right-hand edge of the lower-frequency panels of Figure 14 is actually the previous SNR from the survey, Puppis A.

At frequencies above 70 GHz, the SNR is confused with unrelated emission from cold molecular clouds and cold cores. However, some synchrotron features remain visible

at higher frequencies. The relatively bright feature near the lower centre of the image is Vela-X, the bright nest part of the radio SNR. This feature can be traced all the way to 353 GHz, with contrast steadily decreasing at higher and higher frequencies. Some dust-dominated features are visible at low frequencies. The bright feature at the centre-top of the low-frequency panels of Figure 14 overlap with the very prominent set of knots and filaments in the high-frequency images, with a steadily *decreasing* brightness for the knots and filaments. At frequencies above 100 GHz, the dust features dominate here, while at 30–70 GHz the synchrotron from the SNR dominates.

The 30–70 GHz *Planck* flux densities follow an extrapolation of the radio power law with slightly higher spectral index, indicating the microwave emission mechanism is synchrotron, with no evidence for a spectral break.

3.12. PKS 1209-51/52

The barrel-shaped (Kesteven & Caswell 1987) SNR PKS1209-51/52 is detected by *Planck* at low frequencies. The angular structure of the SNR overlaps in spatial scales with the CMB, so PKS1209-51/52 was masked in the CMB maps. Therefore, Figure 15 shows the total intensity for this SNR, rather than the CMB-subtracted intensity. At 30–70 GHz, the SNR is clearly evident because it is significantly brighter than the CMB and has the location and size seen in lower-frequency radio images. At 100–217 GHz, the SNR is lost in CMB fluctuations. At 353–857 GHz, the region is dominated by interstellar dust emission. The object near the centre of the SNR in the high-frequency images is a reflection nebula, identified by Brand et al. (1986, object 381) on optical places as a $3'$ possible reflection nebula; it was also noted as a far-infrared source without corresponding strong H I emission (Reach et al. 1993, object 9095). There is no evidence for this object to be associated with the SNR nor the neutron star suspected to be the remnant of the progenitor (Vasisht et al. 1997, X-ray source 1E 1207.4-5209), located $12'$ away. It is nonetheless remarkable that the source is right at the centre of the SNR.

Figure 15 shows the low-frequency emission seen by *Planck* continues the radio synchrotron spectrum closely up to 70 GHz, with no evidence for a spectral break.

3.13. RCW 86

The RCW 86 supernova remnant, possibly that of a Type I SN within a stellar wind bubble (Williams et al. 2011), is evident in the low-frequency 30–70 GHz *Planck* images. At higher frequencies the synchrotron emission from the SNR is confused with other emission. The feature near the left-centre of the highest 6 frequency images of RCW 86 in Fig. 16 is a dark molecular cloud, DB 315.7-2.4 (Dutra & Bica 2002). The *Planck* emission from this location is due to dust, with brightness steadily increasing with frequency over the *Planck* domain. The cloud is located near the edge of the SNR, and the CO velocity (-37 km s^{-1}; Otrupcek et al. 2000) is approximately as expected for a cloud at the distance estimate for the SNR (2.3 kpc). Any relation between the cold molecular cloud and the SNR is only plausible; there is no direct evidence for interaction. In any event, the dust in this cloud makes it impossible to measure the synchrotron brightness at 100 GHz, and the 70 GHz flux has higher uncertainty.

For the SNR synchrotron emission, the *Planck* flux densities, shown in Fig. 16, are consistent within 1σ with an extrapolation of the radio synchrotron power law. The existence of X-ray synchrotron emission (Rho et al. 2002) suggests that the energy distribution of relativistic electrons continues to high energy.

3.14. MSH 15-56

The radio-bright SNR MSH 15-5*6* is well detected in the first five *Planck* frequencies, 30–143 GHz. The SNR is a 'composite,' with a steep-spectrum shell and a brighter, flat-spectrum plerionic core. The *Planck* flux densities do not follow a single power law matching the published radio flux densities. Just connecting the 1 GHz radio flux densities to the *Planck* flux densities, the spectral index is in the range 0.3–0.5. The *Planck* flux densities themselves follow a steeper power law than can match the radio flux densities, and suggest a break in the spectral index. Figure 17 shows a broken-power-law fit, where the spectral index steepens from 0.31 to 0.9 at 30 GHz. Low-frequency radio observations show that the plerionic core of the SNR has a flatter spectral index than the shell, while higher-frequency flux densities of the core alone from 4.8 to 8.6 GHz have a spectral index of 0.85 (Dickel et al. 2000). The relatively flat spectral index at radio frequencies and up to about 30 GHz may indicate injection of fresh electrons, as in the Crab and 3C 58, which are driven by pulsar wind nebulae. However, there has been, to date, no pulsar detected in MSH 15-5*6*, and the spectral index is not as flat as in the known, young pulsar wind nebulae. The apparent break in spectral index to a stepper slope above 30 GHz suggests possible energy loss of the highest-energy particles.

3.15. SN 1006

SN 1006 is well-detected at 30–44 GHz. At higher frequencies it becomes faint and possibly confused with unrelated emission. However, the field is not as crowded as it is for most other SNRs, and we suspect that the observed decrement in flux density below the extrapolation of the radio power law at 70 and 100 GHz may be due to a real break in the spectral index. If so, then the frequency of that break is in the range $20 < \nu_{\mathrm{break}} < 30$ GHz. For illustration, Fig. 18 shows a broken power-law fit with $\nu_{\mathrm{break}} = 22$ GHz, above which the spectral index steepens from $\alpha = 0.5$ to $\alpha = 1$ as predicted for synchrotron losses. The *Planck* data appear to match this model well.
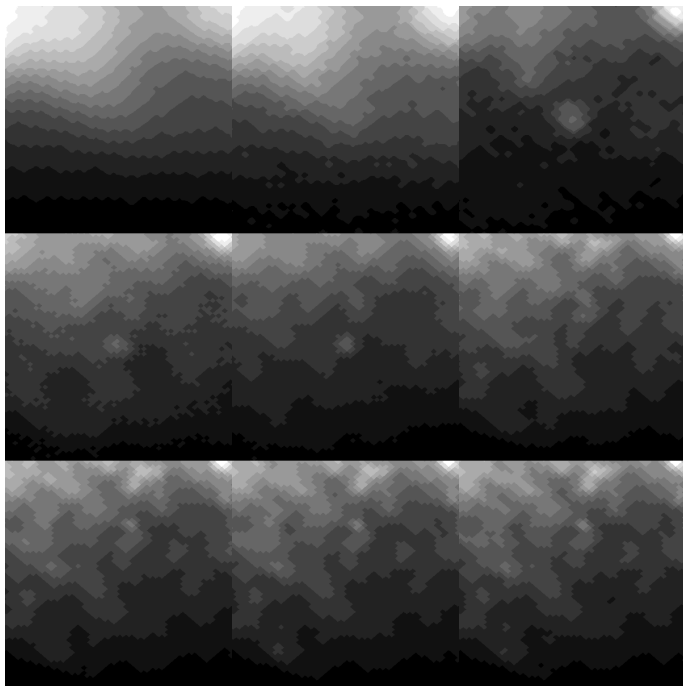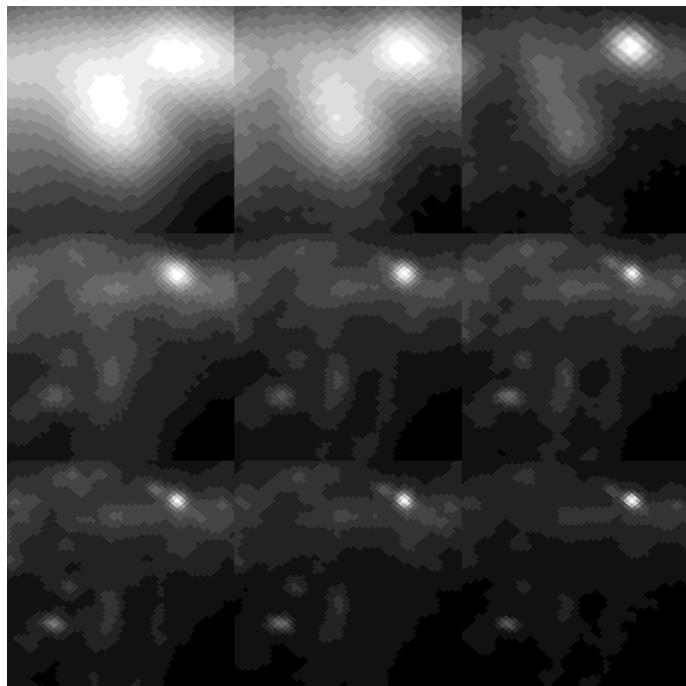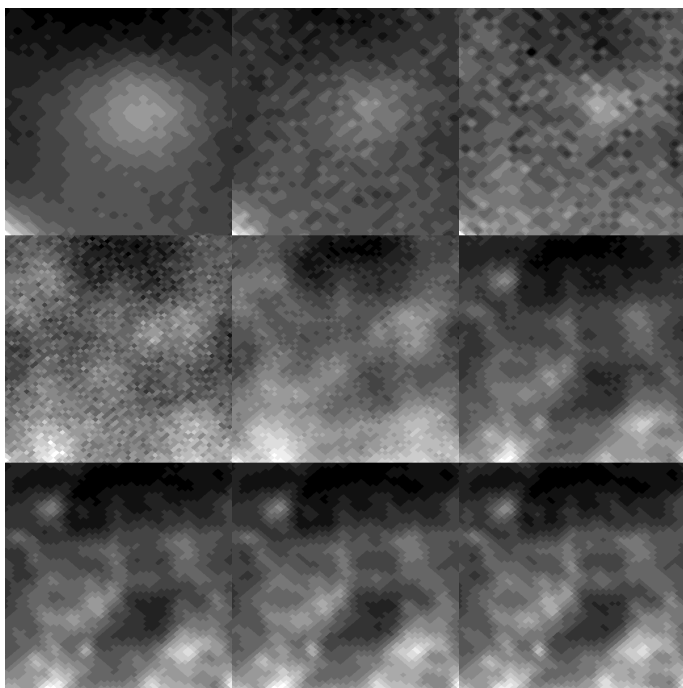
Fig. 2. *Top*: Images of the G21.5-0.9 environment at the nine *Planck* frequencies (Table 1), increasing from 30 GHz at top left to 857 GHz at bottom right. Each image is $100'$ on a side, with galactic coordinate orientation. *Bottom*: Microwave SED of G21.5-0.9. Filled circles are *Planck* measurements from this paper, with 3σ error bars. The open symbol at 1 GHz is from the Green catalogue. The dashed line emanating from the 1 GHz flux density is a flat spectrum, for illustration. The dotted line is a broken power law, with a break frequency at 40 GHz, a spectral index of 0.05 at lower frequencies and 0.55 at higher frequencies. Open diamonds show prior radio flux densities from Morsi & Reich (1987) and Salter et al. (1989).
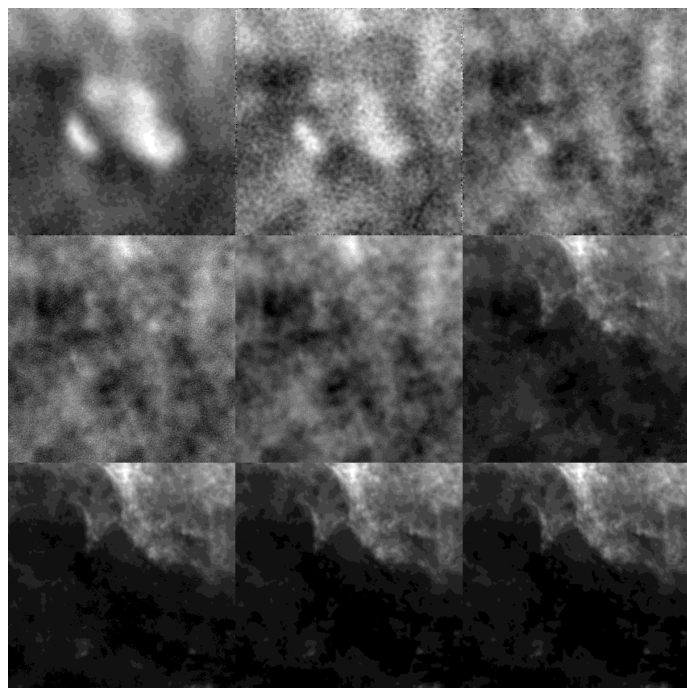
Fig. 3. *Top*: Images of the W 44 environment at the nine *Planck* frequencies (Table 1), increasing from 30 GHz at top left to 857 GHz at bottom right. Each image is $100'$ on a side, with galactic coordinate orientation. *Bottom*: Microwave SED of W 44. Filled circles are *Planck* measurements from this paper, with 3σ error bars. The open symbol at 1 GHz is from the Green catalogue, and the dashed line emanating from it is a power law with spectral index from the Green catalogue. Open diamonds are radio flux densities from Velusamy et al. (1976) at 2.7 GHz, Sun et al. (2011) at 5 GHz and Kundu & Velusamy (1972) at 10.7 GHz. The dotted line illustrates a spectral break increasing the spectral index by 0.5 at 45 GHz to match the *Planck* 70 GHz flux density. Downward arrows show the flux density measurements that are contaminated by unrelated foreground emission.

Fig. 4. *Top*: Images of the CTB 80 environment at the nine *Planck* frequencies (Table 1), increasing from 30 GHz at top left to 857 GHz at bottom right. Each image is 100′ on a side, with galactic coordinate orientation. *Bottom*: Microwave SED of CTB 80. Filled circles are *Planck* measurements from this paper, with 3σ error bars. The open symbol at 1 GHz is from the Green catalogue, and the dashed and dotted line emanating from it are power laws with spectral indices of 0.5 (Green catalogue) and 0.8 (approximate fit for 1–100 GHz), respectively, for illustration. Open diamonds are radio flux densities from Velusamy et al. (1976) at 0.75, 1.00 GHz; Mantovani et al. (1985) at 1.41, 1.72, 2.695 and 4.75 GHz; and Sofue et al. (1983) at 10.2 GHz. The downward arrow shows a flux density measurement that was contaminated by unrelated foreground emission.

Fig. 5. *Top*: Images of the Cygnus Loop environment at the nine *Planck* frequencies (Table 1), increasing from 30 GHz at top left to 857 GHz at bottom right. Each image is 435′ on a side, with galactic coordinate orientation. The SNR is clearly visible in the lowest-frequency images, but a nearby star-forming region (to the north) confuses the SNR at frequencies above 100 GHz. *Bottom*: Spectral energy distribution of the Cygnus Loop including fluxes measured by us from WMAP using the same apertures as for *Planck*, and independent measurements from Uyanıker et al. (2004) and Reich et al. (2003). The dashed curve is a power law normalized through the radio fluxes.
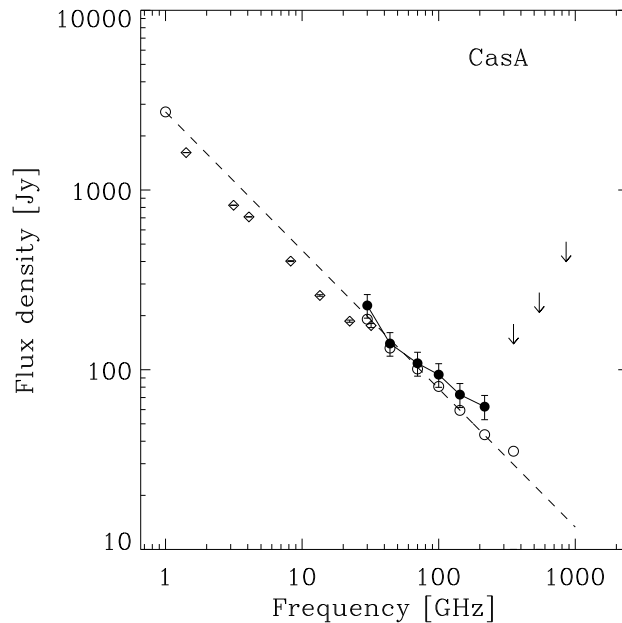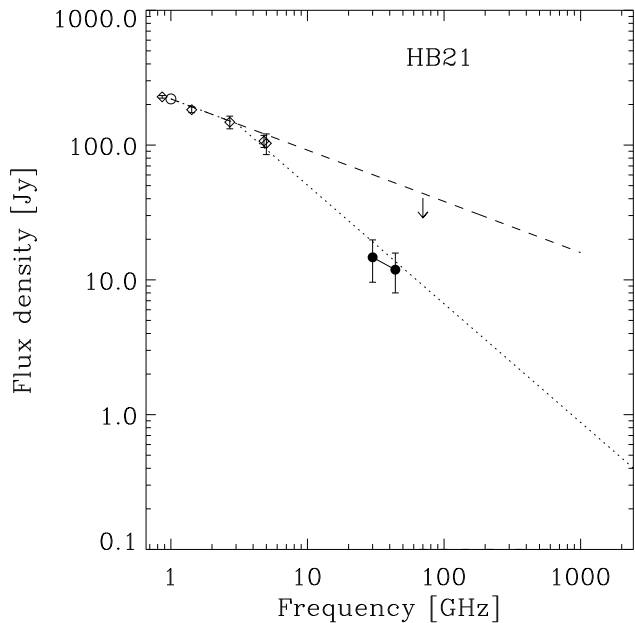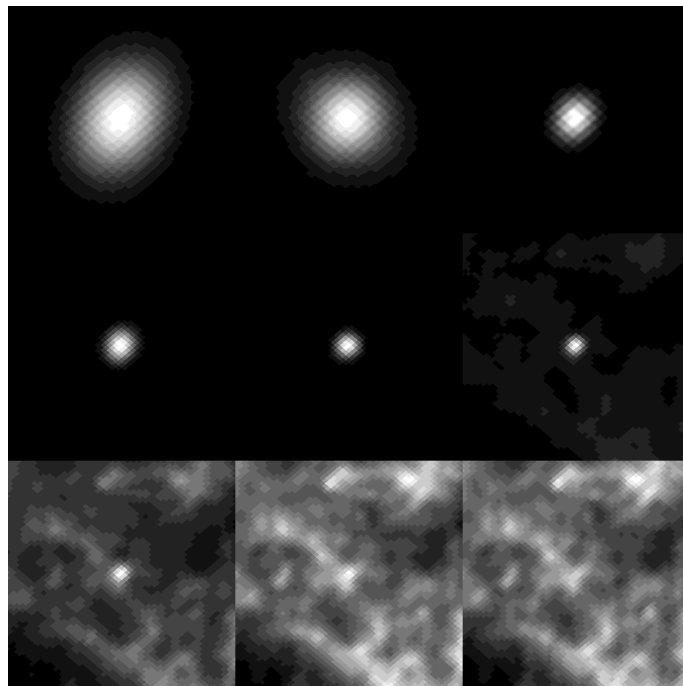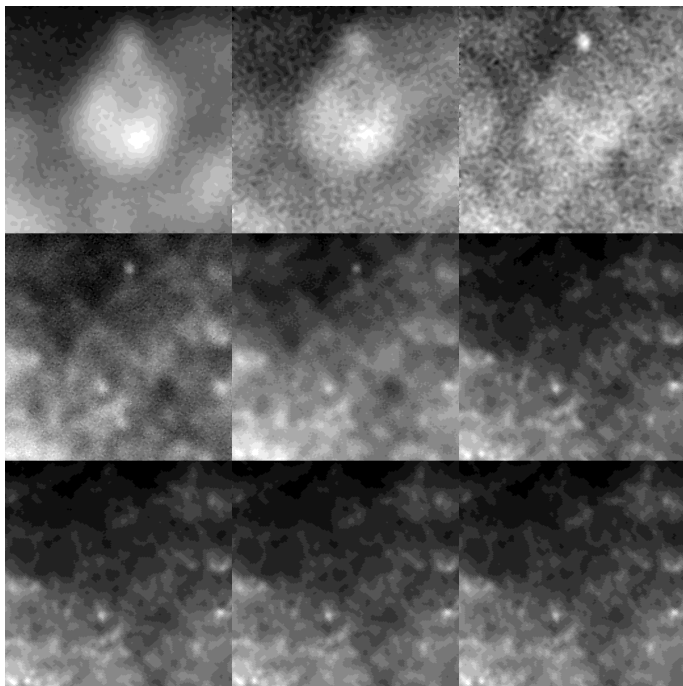
11

Fig. 6. *Top*: Images of the HB 21 environment at the nine *Planck* frequencies (Table 1), increasing from 30 GHz at top left to 857 GHz at bottom right. Each image is 233′ on a side, with galactic coordinate orientation. *Bottom*: Microwave SED of HB 21. Filled circles are *Planck* measurements from this paper, with 3σ error bars. The open symbol at 1 GHz is from the Green catalogue, and the dashed line emanating from it is a power law with spectral index from the Green catalogue. The dotted line is a broken power-law model discussed in the text. Open diamonds are radio flux densities from Reich et al. (2003), Willis (1973), Kothes et al. (2006), and Gao et al. (2011). The downward arrow shows a flux density measurement that was contaminated by unrelated foreground emission.
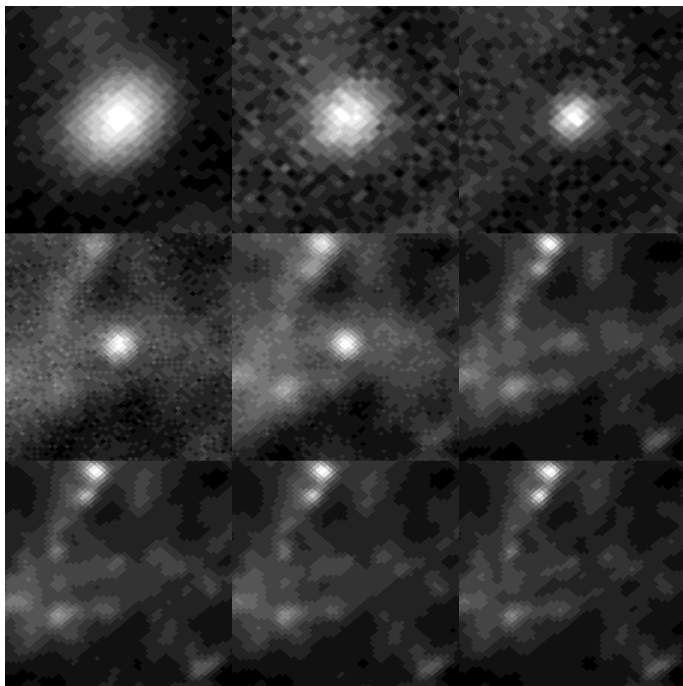
Fig. 7. *Top*: Images of the Cas A environment at the nine *Planck* frequencies (Table 1), increasing from 30 GHz at top left to 857 GHz at bottom right. Each image is 100′ on a side, with galactic coordinate orientation. *Bottom*: Microwave SED of Cas A. Filled circles are *Planck* measurements from this paper, with 3σ error bars. The open symbol at 1 GHz is from the Green catalogue, and the dashed line emanating from it is a power law with spectral index from the Green catalogue. Open circles show the flux densities from the ERCSC, the compilation by Baars et al. (1977) and Mason et al. (1999), after scaling for secular fading to the epoch of the *Planck* observations.

Fig. 8. *Top*: Images of the Tycho SNR environment at the nine *Planck* frequencies (Table 1), increasing from 30 GHz at top left to 857 GHz at bottom right. Each image is 100′ on a side , with galactic coordinate orientation. *Bottom*: Microwave SED of Tycho. Filled circles are *Planck* measurements from this paper, with 3σ error bars. The open symbol at 1 GHz is from the Green catalogue, and the dashed line emanating from it is a power law with spectral index from the Green catalogue. Open diamonds are a 10.7 GHz measurement from Klein et al. (1979) and *Herschel* flux density from Gomez et al. (2012). The dotted lines are a revised synchrotron power law with spectral index $\alpha = 0.6$ at low frequency, based on the radio including 10.7 GHz and the *Planck* 30–143 GHz flux densities, and a modified blackbody with emissivity index $\beta = 1$ and temperature 21 K at high frequency, based on the *Herschel* data. Downward arrows are upper limits (99.5% confidence) to the flux density from high-frequency *Planck* data. The solid line is a combination of the synchrotron and dust models.
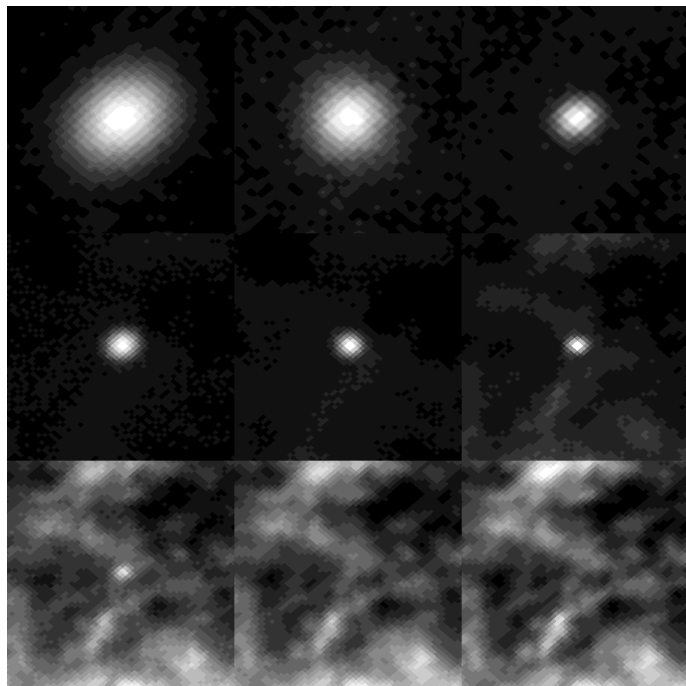
Fig. 9. *Top*: Images of the 3C 58 environment at the nine *Planck* frequencies (Table 1), increasing from 30 GHz at top left to 857 GHz at bottom right. Each image is 100′ on a side,with galactic coordinate orientation. *Bottom*: Microwave SED of 3C 58. Filled circles are *Planck* measurements from this paper, with 3σ error bars. The open symbol at 1 GHz is from the Green catalogue, and the dashed line emanating from it is a power law with spectral index from the Green catalogue. Open circles are from the *Planck* ERCSC. Diamonds show published flux densities: Salter et al. (1989) measured 15 ± 2 Jy at 84.2 GHz; Morsi & Reich (1987) measured 25.2 ± 1.4 Jy at 32 GHz; Green et al. (1975) measured 26.7 ± 0.5 Jy at 15 GHz; and Green (1986) measured 30 ± 3 Jy at 2.7 GHz. Flux densities from Weiland et al. (2011) are also included as open diamonds, together with a solid line showing a fit to their data. The dotted line is the broken power-law model for a pulsar wind nebula with energy injection spectrum matching the radio (low-frequency) data and a break at 25 GHz due to synchrotron cooling (see Sect. 3.8).
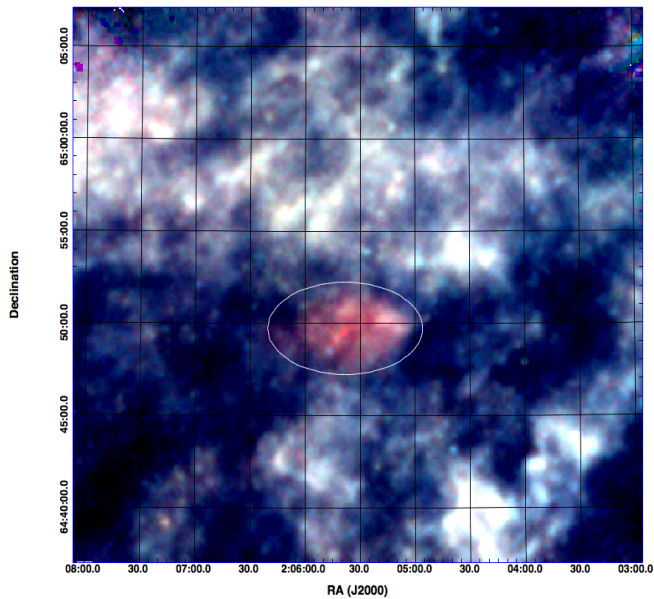
13

Fig. 10. Multi-colour *Herschel*/SPIRE image of 3C 58 created from images at $510\,\mu$m (587 GHz; red), $350\,\mu$m (857 GHz; green) and $250\,\mu$m (1200 GHz; blue). A white ellipse of $9' \times 5'$ diameter shows the size of the radio SNR. The diffuse interstellar medium is mostly white in this image, while the emission within the ellipse is distinctly red, being brightest at $510\,\mu$m while the diffuse interstellar medium is brightest at $250\,\mu$m. The red, compact source at the centre of the ellipse is coincident with PSR J0205+6449 that is thought to be the compact remnant of the progenitor star.
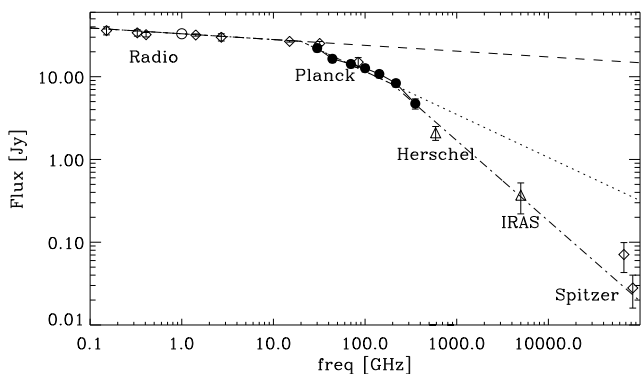

Fig. 11. Microwave SED of 3C 58 from the radio through infrared. Data are as in Fig. 9 with the addition of lower-frequency radio flux densities (Green 2009) and higher-frequency *IRAS* and *Spitzer* flux densities, and omission of the ERCSC flux densities. The dashed line is the power-law fit to the radio flux densities; the dotted line is the pulsar wind nebula model; and the dash-dotted line is that model with the addition of a second break with spectral index 0.92 above 200 GHz.
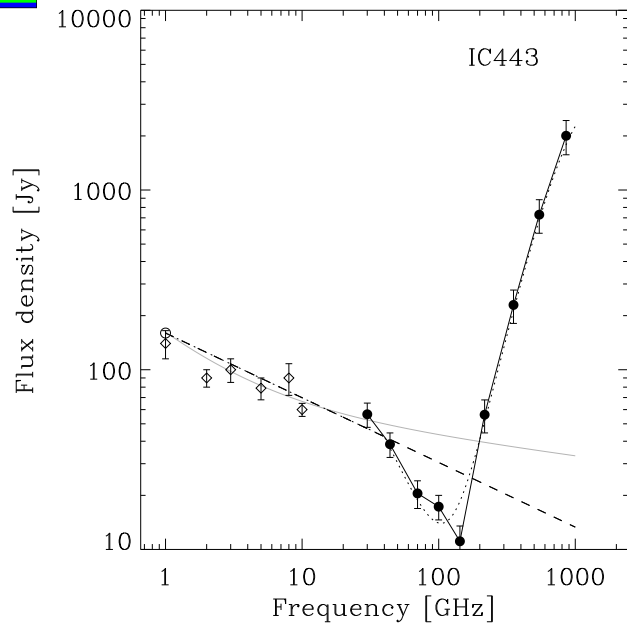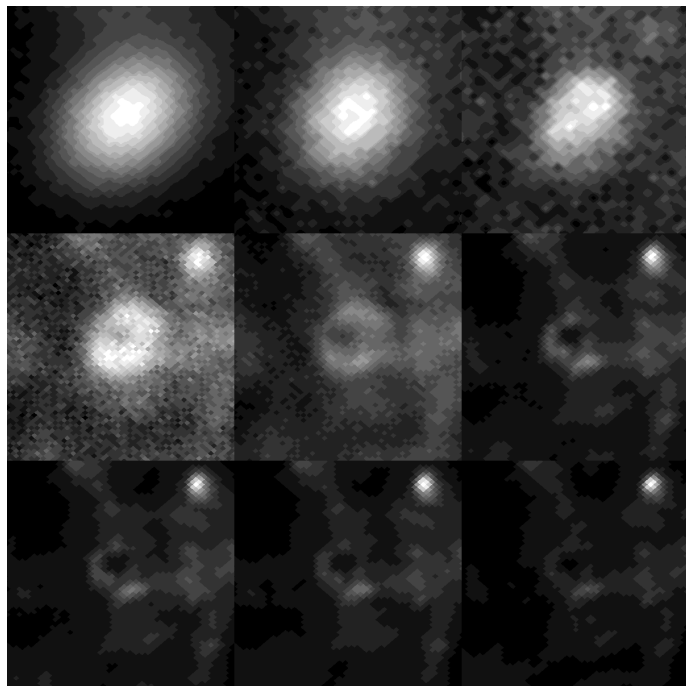

Fig. 12. *Top*: Images of the IC 443 environment at the nine *Planck* frequencies (Table 1), increasing from 30 GHz at top left to 857 GHz at bottom right. Each image is $100'$ on a side, with galactic coordinate orientation. *Bottom*: Microwave SED of IC 443. Filled circles are *Planck* measurements from this paper, with 3σ error bars. The open symbol at 1 GHz is from the Green catalogue, and the dashed line emanating from it is a power law with spectral index from the Green catalogue. Open diamonds are other radio flux densities from the compilation by Castelletti et al. (2011). The dotted line is a model (dust plus broken-power-law synchrotron) discussed in the text in §3.9. The solid grey curve is an extrapolation from Onić et al. (2012).
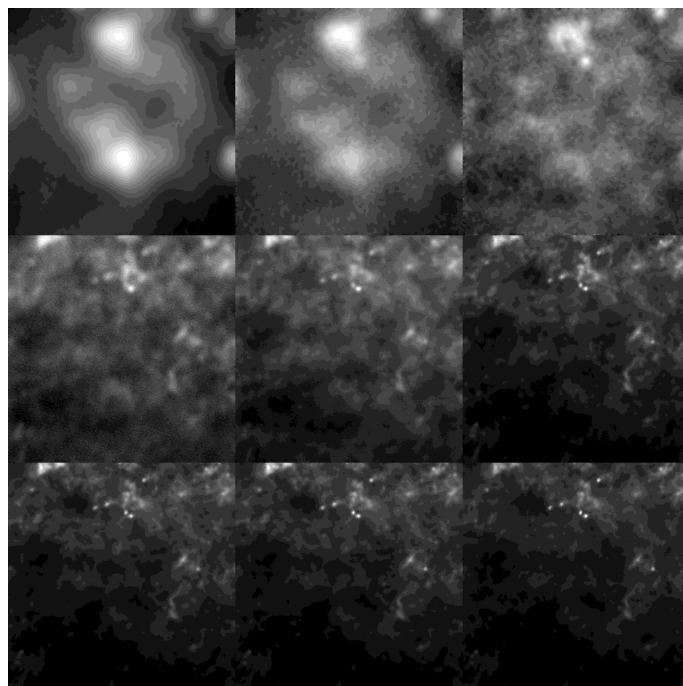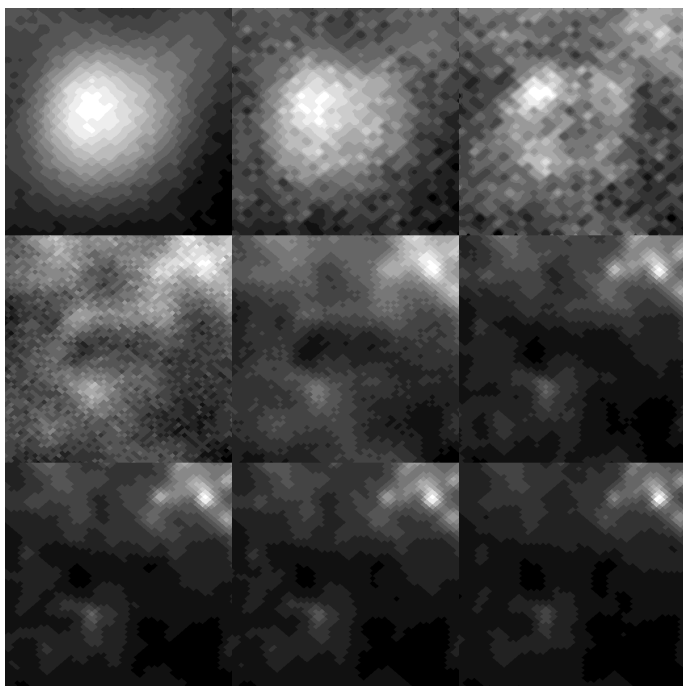
Fig. 13. *Top*: Images of the Puppis A environment at the nine *Planck* frequencies (Table 1), increasing from 30 GHz at top left to 857 GHz at bottom right. Each image is $100'$ on a side, with galactic coordinate orientation. *Bottom*: Microwave SED of Puppis A. Filled circles are *Planck* measurements from this paper, with 3σ error bars. The open symbol at 1 GHz is from the Green catalogue, and the dashed line emanating from it is a power law with spectral index from the Green catalogue. Open diamonds are radio flux densities from the Milne et al. (1993) and *WMAP* fluxes from Hewitt et al. (2012).

Fig. 14. *Top*: Images of the Vela environment at the nine *Planck* frequencies (Table 1), increasing from 30 GHz at top left to 857 GHz at bottom right. Each image is $400'$ on a side, with galactic coordinate orientation, centred 1° north of Vela-X. *Bottom*: Microwave SED of Vela. Filled circles are *Planck* measurements from this paper, with 3σ error bars. The open symbol at 1 GHz is from the Green catalogue, and the dashed line emanating from it is a power law with spectral index from the Green catalogue. Downward arrows show the *Planck* high-frequency flux density measurements that are contaminated by unrelated foreground emission.
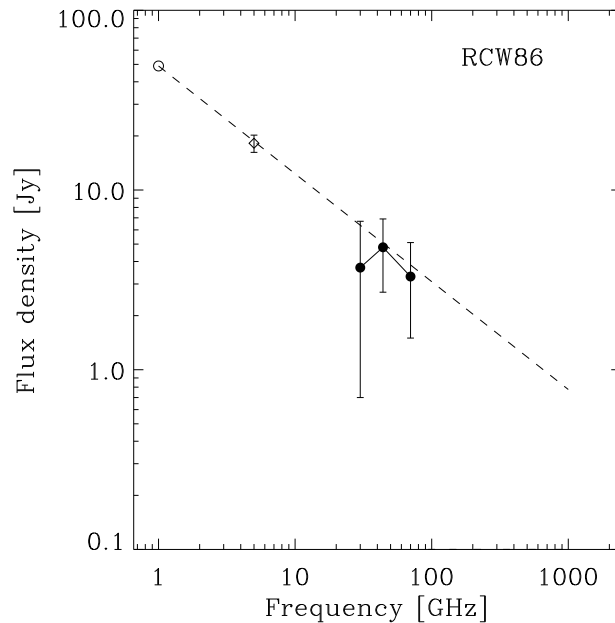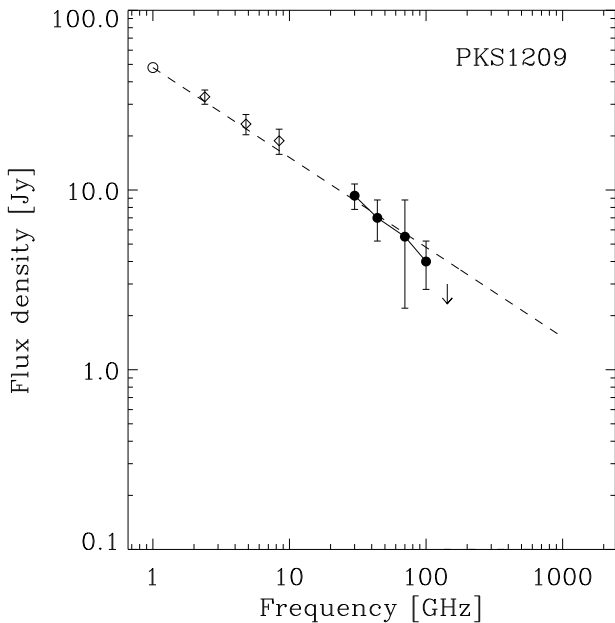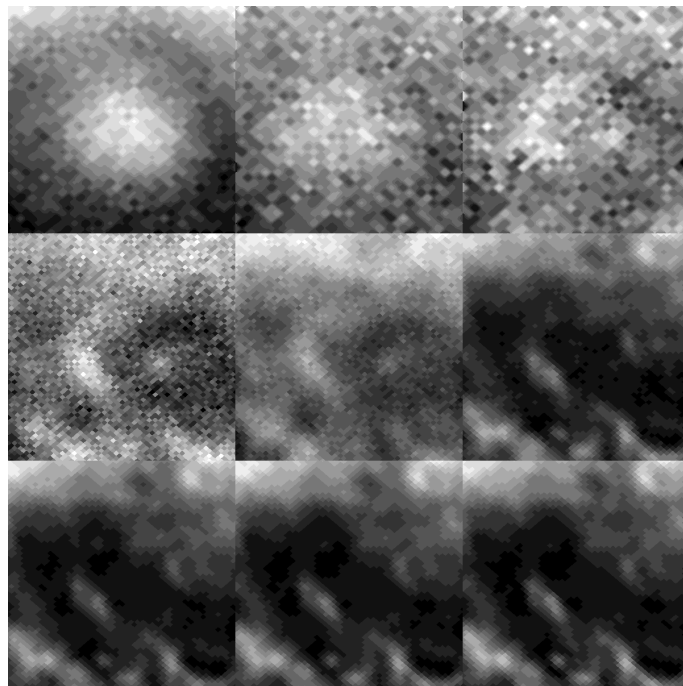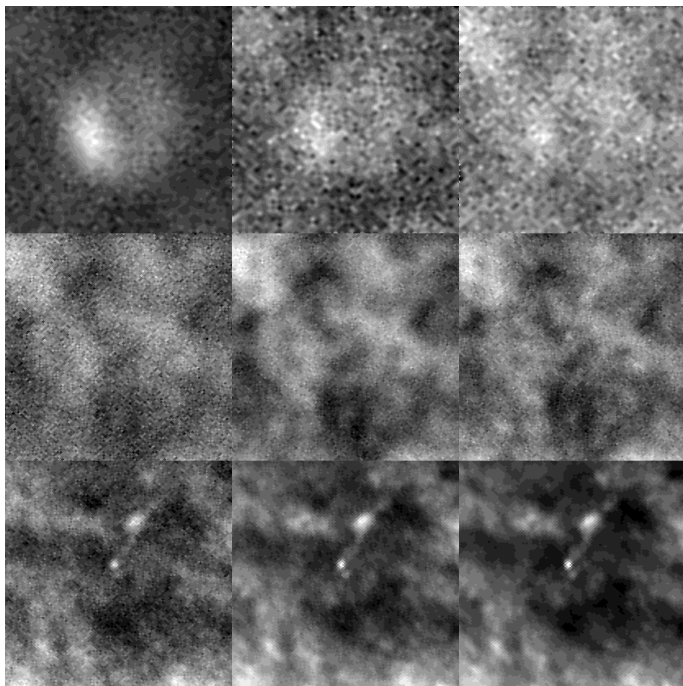
Fig. 15. *Top*: Images of the PKS 1209-51/52 environment at the nine *Planck* frequencies (Table 1), increasing from 30 GHz at top left to 857 GHz at bottom right. Each image is 180′ on a side, with galactic coordinate orientation. *Bottom*: Microwave SED of PKS 1209-52. Filled circles are *Planck* measurements from this paper, with 3σ error bars. The open symbol at 1 GHz is from the Green catalogue, and the dashed line emanating from it is a power law with spectral index from the Green catalogue. Open diamonds are radio flux densities from Milne & Haynes (1994). The downward arrow shows a *Planck* high-frequency flux density measurement that was contaminated by unrelated foreground emission.

Fig. 16. *Top*: Images of the RCW 86 environment at the nine *Planck* frequencies (Table 1), increasing from 30 GHz at top left to 857 GHz at bottom right. Each image is 100′ on a side, with galactic coordinate orientation. *Bottom*: Microwave SED of RCW 86. Filled circles are *Planck* measurements from this paper, with 3σ error bars. The open symbol at 1 GHz is from the Green catalogue, and the dashed line emanating from it is a power law with spectral index from the Green catalogue. The open diamonds is the 5 GHz flux density from Caswell et al. (1975).
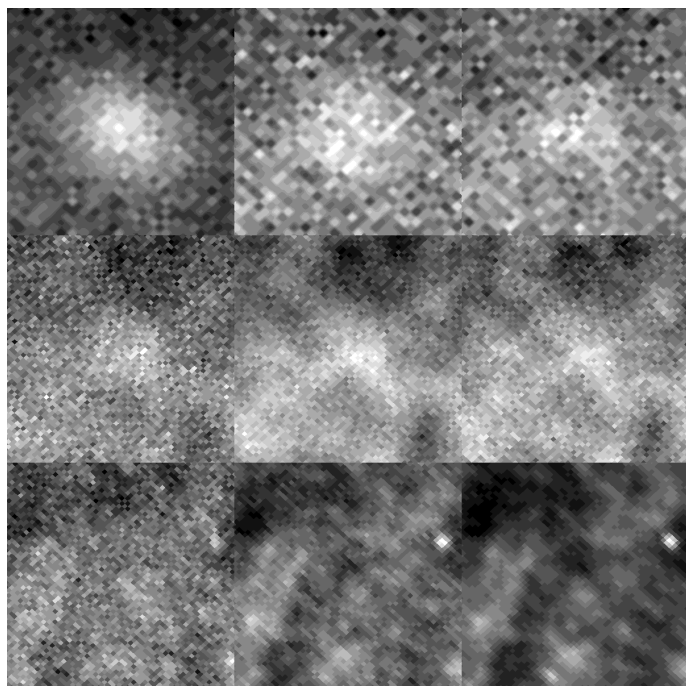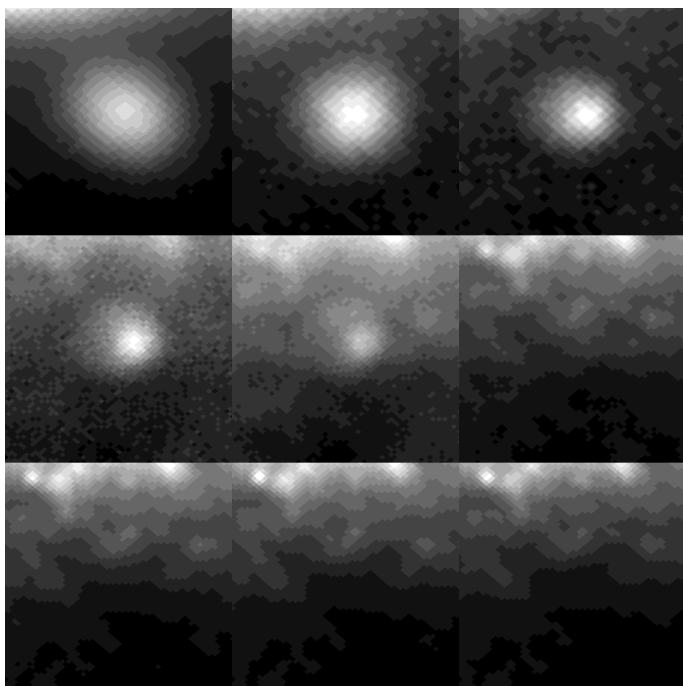
Fig. 17. *Top*: Images of the MSH 15-5*6* environment at the nine *Planck* frequencies (Table 1), increasing from 30 GHz at top left to 857 GHz at bottom right. Each image is 100′ on a side, with galactic coordinate orientation. *Bottom*: Microwave SED of MSH 15-5*6*. Filled circles are *Planck* measurements from this paper, with 3σ error bars. The open symbol at 1 GHz is from the Green catalogue, and the dashed line emanating from it is a power law with spectral index from the Green catalogue. Open diamonds are radio flux densities from the Dickel et al. (2000) and Milne et al. (1979) that constrain the slope through the *Planck* data.

Fig. 18. *Top*: Images of the SN 1006 environment at the nine *Planck* frequencies (Table 1), increasing from 30 GHz at top left to 857 GHz at bottom right. Each image is 100′ on a side, with galactic coordinate orientation. *Bottom*: Microwave SED of SN 1006. Filled circles are *Planck* measurements from this paper, with 3σ error bars. The open symbol at 1 GHz is from the Green catalogue, and the dashed line emanating from it is a power law with spectral index from the Green catalogue. The dotted line is a broken power-law fit discussed in the text.

Table 5. Sychrotron spectral indices

SNR	Spectral index		ν_{break}
	α_1	α_2	[GHz]
G21.5-0.9 ..	0.05	0.55	45
W 44	0.37	1.37	45
CTB 80 ...	0.80	...	none
HB 21	0.38	0.88	3
3C 58	0.07	0.57	25
IC 443	0.36	1.56	40
Puppis A ..	0.46	1.46	40
MSH 15-5*6* .	0.31	0.9	30
SN 1006 ...	0.50	1.0	22

4. Conclusions

The flux densities of 16 known Galactic supernova remnants were measured from the *Planck* microwave all-sky survey with the following conclusions. We find new evidence for spectral index breaks in G21.5-0.9, HB 21, MSH 15-5*6*, SN 1006, and we confirm the previously detected spectral break in 3C 58, including a new detection with *Herschel*.

Table 5 summarizes the new spectral indices required to fit the radio through microwave SED of SNRs. These values correspond to the dashed lines in the SEDs for each SNR in this paper. For each SNR in this paper for which the *Planck* data indicated in a spectrum noticeably different from the radio power-law extrapolation, the frequency of the spectral break (ν_{break}) and the spectral index at lower and higher frequencies (α_1 and α_2, respectively) are listed. The actual SEDs should be consulted before using the spectral index values by themselves, because they are only applicable over the region shown, and they are only mathematical approximations to what is more likely a continuous distribution of energies with evolving losses.

The breaks in spectral index are consistent with synchrotron losses of electrons injected by a central source. We extend the radio synchrotron spectrum for young SNRs Cas A and Tycho with no evidence for extra emission mechanisms. The distinction in properties between those supernova remnants that do or do not show a break in their power-law spectral index is not readily evident. The supernova remnants with spectral breaks include examples that range from bright to faint and young to mature, and they also include examples both with and without stellar remnants. A combination of cosmic-ray acceleration by the shocks and the pulsars, deceleration in denser environments, and ageing may lead to the variation in synchrotron shapes.

References

AMI Consortium, Perrott, Y. C., Green, D. A., et al. 2012, MNRAS, 421, L6

Arendt, R. G., Dwek, E., & Leisawitz, D. 1992, ApJ, 400, 562

Ashworth, Jr., W. B. 1980, Journal for the History of Astronomy, 11, 1

Aumann, H. H., Fowler, J. W., & Melnyk, M. 1990, AJ, 99, 1674

Baars, J. W. M., Genzel, R., Pauliny-Toth, I. I. K., & Witzel, A. 1977, A&A, 61, 99

Barlow, M. J., Krause, O., Swinyard, B. M., et al. 2010, A&A, 518, L138

Bersanelli, M., Mandolesi, N., Butler, R. C., et al. 2010, A&A, 520, A4

Bietenholz, M. F. & Bartel, N. 2008, MNRAS, 386, 1411

Brand, J., Blitz, L., & Wouterloot, J. G. A. 1986, A&AS, 65, 537

Camilo, F., Ransom, S. M., Gaensler, B. M., et al. 2006, ApJ, 637, 456

Castelletti, G., Dubner, G., Clarke, T., & Kassim, N. E. 2011, A&A, 534, A21

Castelletti, G., Dubner, G., Golap, K., et al. 2003, AJ, 126, 2114

Caswell, J. L., Clark, D. H., & Crawford, D. F. 1975, Australian Journal of Physics Astrophysical Supplement, 37, 39

Dickel, J. R., Milne, D. K., & Strom, R. G. 2000, ApJ, 543, 840

Dutra, C. M. & Bica, E. 2002, A&A, 383, 631

Gao, X. Y., Han, J. L., Reich, W., et al. 2011, A&A, 529, A159

Gomez, H. L., Clark, C. J. R., Nozawa, T., et al. 2012, MNRAS, 420, 3557

Górski, K. M., Hivon, E., Banday, A. J., et al. 2005, ApJ, 622, 759

Green, A. J., Baker, J. R., & Landecker, T. L. 1975, A&A, 44, 187

Green, D. A. 1986, MNRAS, 218, 533

Green, D. A. 2009, Bulletin of the Astronomical Society of India, 37, 45 (Green catalogue)

Green, D. A. & Scheuer, P. A. G. 1992, MNRAS, 258, 833

Gupta, Y., Mitra, D., Green, D. A., & Acharyya, A. 2005, Current Science, 89, 853

Han, J. L., Reich, W., Sun, X. H., et al. 2013, International Journal of Modern Physics Conference Series, 23, 82

Hewitt, J. W., Grondin, M.-H., Lemoine-Goumard, M., et al. 2012, ApJ, 759, 89

Kesteven, M. J. & Caswell, J. L. 1987, A&A, 183, 118

Klein, U., Emerson, D. T., Haslam, C. G. T., & Salter, C. J. 1979, A&A, 76, 120

Kothes, R., Fedotov, K., Foster, T. J., & Uyanıker, B. 2006, A&A, 457, 1081

Kundu, M. R. & Velusamy, T. 1972, A&A, 20, 237

Lamarre, J., Puget, J., Ade, P. A. R., et al. 2010, A&A, 520, A9

Macías-Pérez, J. F., Mayet, F., Aumont, J., & Désert, F.-X. 2010, ApJ, 711, 417

Mandolesi, N., Bersanelli, M., Butler, R. C., et al. 2010, A&A, 520, A3

Mantovani, F., Reich, W., Salter, C. J., & Tomasi, P. 1985, A&A, 145, 50

Mason, B. S., Leitch, E. M., Myers, S. T., Cartwright, J. K., & Readhead, A. C. S. 1999, AJ, 118, 2908

McCray, R. & Wang, Z., eds. 1996, Supernovae and Supernova Remnants: IAU Colloquium 145 (Cambridge University Press)

Mennella, A., Butler, R. C., Curto, A., et al. 2011, A&A, 536, A3

Milne, D. K., Goss, W. M., Haynes, R. F., et al. 1979, MNRAS, 188, 437

Milne, D. K. & Haynes, R. F. 1994, MNRAS, 270, 106

Milne, D. K., Stewart, R. T., & Haynes, R. F. 1993, MNRAS, 261, 366

Morsi, H. W. & Reich, W. 1987, A&AS, 69, 533

Onić, D., Urošević, D., Arbutina, B., & Leahy, D. 2012, ApJ, 756, 61

Otrupcek, R. E., Hartley, M., & Wang, J.-S. 2000, PASA, 17, 92

Pivato, G., Hewitt, J. W., Tibaldo, L., et al. 2013, ApJ, 779, 179

Planck HFI Core Team. 2011a, A&A, 536, A4

Planck HFI Core Team. 2011b, A&A, 536, A6

Planck Collaboration I. 2011, A&A, 536, A1

Planck Collaboration II. 2011, A&A, 536, A2

Planck Collaboration VII. 2011, A&A, 536, A7 (ERCSC)

Planck Collaboration IV. 2014, A&A, 571, A4

Planck Collaboration V. 2014, A&A, 571, A5

Planck Collaboration VII. 2014, A&A, 571

Planck Collaboration VIII. 2014, A&A, 571, A8

Planck Collaboration XII. 2014, A&A, 571, A12

Reach, W. T., Heiles, C., & Koo, B.-C. 1993, ApJ, 412, 127

Reich, W., Zhang, X., & Fürst, E. 2003, A&A, 408, 961

Reynolds, S. P. 2009, ApJ, 703, 662

Reynolds, S. P. 2011, Ap&SS, 336, 257

Rho, J., Dyer, K. K., Borkowski, K. J., & Reynolds, S. P. 2002, ApJ, 581, 1116

Rho, J., Jarrett, T. H., Cutri, R. M., & Reach, W. T. 2001, ApJ, 547, 885

Salter, C. J., Reynolds, S. P., Hogg, D. E., Payne, J. M., & Rhodes, P. J. 1989, ApJ, 338, 171

Scaife, A., Green, D. A., Battye, R. A., et al. 2007, MNRAS, 377, L69

Slane, P., Helfand, D. J., Reynolds, S. P., et al. 2008, ApJ, 676, L33

Sofue, Y., Takahara, F., Hirabayashi, H., Inoue, M., & Nakai, N. 1983, PASJ, 35, 437

Sun, X. H., Reich, P., Reich, W., et al. 2011, A&A, 536, A83

Sun, X. H., Reich, W., Han, J. L., Reich, P., & Wielebinski, R. 2006, A&A, 447, 937

Tauber, J. A., Mandolesi, N., Puget, J., et al. 2010, A&A, 520, A1

Uyanıker, B., Reich, W., Yar, A., & Fürst, E. 2004, A&A, 426, 909

Vasisht, G., Kulkarni, S. R., Anderson, S. B., Hamilton, T. T., & Kawai, N. 1997, ApJ, 476, L43

Velusamy, T., Kundu, M. R., & Becker, R. H. 1976, A&A, 51, 21

Weiland, J. L., Odegard, N., Hill, R. S., et al. 2011, ApJS, 192, 19

Williams, B. J., Blair, W. P., Blondin, J. M., et al. 2011, ApJ, 741, 96

Willis, A. G. 1973, A&A, 26, 237

Zacchei, A., Maino, D., Baccigalupi, C., et al. 2011, A&A, 536, A5

Appendix A: Aperture photometry details

More details on the aperture photometry are provided in Table A.1. For each flux density measurement, the following quantities are listed.

(1) The supernova remnant (SNR) name, in the same order as in Tables 2 and 3.

(2) The observing frequency in GHz.

(3) 'Flux' is the aperture-corrected, background-subtracted flux of the source with its uncertainty. The uncertainty is a quadrature combination of the statistical uncertainty and the flux calibration uncertainty. The flux calibration uncertainty is the flux multiplied by the mission calibration uncertainty from Table 1. The statistical uncertainty is the rms of the pixel values in the background annulus, I_{rms}, multiplied by the number of pixels in the on-source aperture and divided by the square-root of the number of pixels in the off-source annulus, then scaled by the same aperture correction as was applied to the flux.

(4) θ_{ap} is the aperture radius, within which the source flux was summed.

(5) f_A is the aperture correction factor, from equation 2.

(6) F_{bg} is the flux of the background that was subtracted from the on-source sum of the source flux. This was calculated by taking the median brightness within the background annulus, then multiplying by the area of the on-source aperture. To aid direct comparison we also applied the same aperture correction as was applied to the source flux. Because of the line lines of sight through the Galactic disk at the locations of most of the SNRs, the backgrounds are high, and F_{bg} is often higher than the flux of the SNR. In itself, this is not a fundamental limitation, because a smooth background can be much brighter than the target without affecting the photometry.

(7) I_{peak} is the peak intensity in the on-source aperture, in the units of the map for which the photometry was being performed. For frequencies 30–353 GHz, the units are mK in thermodynamic CBM brightness temperature units. For 545–857 GHz, the units are MJy sr^{-1}.

(8) I_{bg} is the median intensity in the background annulus, in the same units units as I_{peak}.

(9) I_{rms} is the standard deviation (rms) of the pixel values in the background annulus, in the same units as I_{peak}. The peak, per-pixel signal-to-noise for each target can be estimated as I_{peak}/I_{rms} because the target causes the brightest pixel in the on-source aperture. This gives a quantitative measure of how readily visible the target is, at the angular scale of the *Planck* beam.

[1] APC, AstroParticule et Cosmologie, Université Paris Diderot, CNRS/IN2P3, CEA/lrfu, Observatoire de Paris, Sorbonne Paris Cité, 10, rue Alice Domon et Léonie Duquet, 75205 Paris Cedex 13, France

[2] Aalto University Metsähovi Radio Observatory and Dept of Radio Science and Engineering, P.O. Box 13000, FI-00076 AALTO, Finland

[3] African Institute for Mathematical Sciences, 6-8 Melrose Road, Muizenberg, Cape Town, South Africa

[4] Agenzia Spaziale Italiana Science Data Center, Via del Politecnico snc, 00133, Roma, Italy

[5] Astrophysics Group, Cavendish Laboratory, University of Cambridge, J J Thomson Avenue, Cambridge CB3 0HE, U.K.

[6] Astrophysics & Cosmology Research Unit, School of Mathematics, Statistics & Computer Science, University of KwaZulu-Natal, Westville Campus, Private Bag X54001, Durban 4000, South Africa

[7] Atacama Large Millimeter/submillimeter Array, ALMA Santiago Central Offices, Alonso de Cordova 3107, Vitacura, Casilla 763 0355, Santiago, Chile

[8] CGEE, SCS Qd 9, Lote C, Torre C, 4° andar, Ed. Parque Cidade Corporate, CEP 70308-200, Brasília, DF, Brazil

[9] CITA, University of Toronto, 60 St. George St., Toronto, ON M5S 3H8, Canada

[10] CNRS, IRAP, 9 Av. colonel Roche, BP 44346, F-31028 Toulouse cedex 4, France

[11] California Institute of Technology, Pasadena, California, U.S.A.

[12] Centro de Estudios de Física del Cosmos de Aragón (CEFCA), Plaza San Juan, 1, planta 2, E-44001, Teruel, Spain

[13] Computational Cosmology Center, Lawrence Berkeley National Laboratory, Berkeley, California, U.S.A.

[14] DSM/Irfu/SPP, CEA-Saclay, F-91191 Gif-sur-Yvette Cedex, France

[15] DTU Space, National Space Institute, Technical University of Denmark, Elektrovej 327, DK-2800 Kgs. Lyngby, Denmark

[16] Département de Physique Théorique, Université de Genève, 24, Quai E. Ansermet,1211 Genève 4, Switzerland

[17] Departamento de Física Fundamental, Facultad de Ciencias, Universidad de Salamanca, 37008 Salamanca, Spain

[18] Departamento de Física, Universidad de Oviedo, Avda. Calvo Sotelo s/n, Oviedo, Spain

[19] Department of Astrophysics/IMAPP, Radboud University Nijmegen, P.O. Box 9010, 6500 GL Nijmegen, The Netherlands

[20] Department of Physics & Astronomy, University of British Columbia, 6224 Agricultural Road, Vancouver, British Columbia, Canada

[21] Department of Physics and Astronomy, Dana and David Dornsife College of Letter, Arts and Sciences, University of Southern California, Los Angeles, CA 90089, U.S.A.

[22] Department of Physics and Astronomy, University College London, London WC1E 6BT, U.K.

[23] Department of Physics, Florida State University, Keen Physics Building, 77 Chieftan Way, Tallahassee, Florida, U.S.A.

[24] Department of Physics, Gustaf Hällströmin katu 2a, University of Helsinki, Helsinki, Finland

[25] Department of Physics, Princeton University, Princeton, New Jersey, U.S.A.

Table A.1. Aperture photometry details for *Planck* flux density measurements of supernova remnants.

(1) Source	(2) Freq. [GHz]	(3) Flux [Jy]	(4) θ_{ap} [']	(5) f_A	(6) F_{bg} [Jy]	(7) I_{peak} [a]	(8) I_{bg} [a]	(9) I_{rms} [a]
G21.5-0.9	70	4.3 ± 0.6	10.2	1.4	7.1	3.1	1.4	0.4
G21.5-0.9	100	2.5 ± 0.5	8.1	1.4	17.6	4.5	3.1	0.5
G21.5-0.9	143	2.9 ± 0.4	6.0	1.4	15.4	4.5	2.9	0.3
W44	30	121.0 ± 8.2	36.1	1.4	149.2	28.6	11.6	5.8
W44	44	67.2 ± 5.2	33.2	1.4	103.1	11.0	4.5	2.2
W44	70	29.5 ± 3.3	28.0	1.0	64.1	5.3	2.3	1.6
CTB80	30	14.5 ± 1.7	64.9	1.0	39.3	3.3	1.3	2.2
CTB80	44	8.4 ± 1.2	63.3	1.0	25.8	1.3	0.4	1.0
CygLoop	30	22.2 ± 1.6	174.3	1.0	61.1	1.3	0.3	0.4
HB21	30	15.4 ± 1.7	93.3	1.0	110.6	3.6	1.8	0.8
HB21	44	10.0 ± 1.2	92.2	1.0	74.8	1.3	0.6	0.3
CasA	30	227.2 ± 11.4	25.0	1.4	15.8	76.8	2.6	1.5
CasA	44	139.7 ± 7.0	20.6	1.4	12.1	33.6	1.4	0.7
CasA	70	108.9 ± 5.5	10.4	1.4	4.4	40.8	0.8	0.7
CasA	100	93.9 ± 4.7	8.4	1.4	5.7	34.5	0.9	0.3
CasA	143	72.7 ± 3.7	6.5	1.4	7.2	28.7	1.2	0.3
CasA	217	62.2 ± 3.2	5.1	1.4	21.4	34.1	4.3	0.6
CasA	353	59.9 ± 3.9	5.0	1.4	82.5	72.8	28.8	3.3
Tycho	30	8.4 ± 0.4	25.5	1.4	10.0	4.3	1.6	0.2
Tycho	44	5.4 ± 0.3	21.1	1.4	5.3	2.0	0.6	0.1
Tycho	70	4.5 ± 0.3	11.4	1.4	2.9	1.9	0.4	0.1
Tycho	100	3.9 ± 0.2	9.6	1.4	6.0	1.9	0.7	0.1
Tycho	143	3.5 ± 0.2	8.0	1.4	9.1	2.0	1.0	0.1
3C58	30	23.7 ± 1.2	25.7	1.4	5.0	8.2	0.8	0.2
3C58	44	17.5 ± 0.9	21.3	1.4	3.2	4.3	0.3	0.1
3C58	70	15.3 ± 0.8	11.9	1.4	2.3	5.5	0.3	0.1
3C58	100	13.8 ± 0.7	10.1	1.4	3.4	4.7	0.4	0.1
3C58	143	11.6 ± 0.6	8.6	1.4	5.9	4.2	0.6	0.1
3C58	217	6.5 ± 0.4	7.6	1.0	11.9	5.1	1.6	0.1
3C58	353	3.6 ± 0.5	7.5	1.0	45.1	14.4	10.4	0.6
Crab	30	425.4 ± 21.3	25.3	1.4	5.9	138.8	0.9	2.5
Crab	44	313.8 ± 15.7	20.9	1.4	10.0	75.4	1.1	1.3
Crab	70	286.7 ± 14.4	11.1	1.4	3.1	107.0	0.5	1.3
Crab	100	278.5 ± 13.9	9.2	1.4	0.8	95.8	0.1	0.4
Crab	143	255.3 ± 12.8	7.4	1.4	2.5	89.0	0.3	0.2
Crab	217	221.5 ± 11.1	6.3	1.4	5.8	108.5	0.9	0.1
Crab	353	197.8 ± 9.9	6.2	1.4	27.6	163.1	6.6	0.3
Crab	545	153.7 ± 7.7	6.2	1.4	89.1	46.0	6.3	0.3
Crab	857	136.9 ± 7.2	6.1	1.4	249.6	57.1	17.8	0.8
IC443	30	56.0 ± 2.8	38.9	1.4	13.9	9.8	0.9	0.8
IC443	44	38.1 ± 2.0	36.2	1.4	11.0	3.9	0.4	0.3
IC443	70	19.5 ± 1.1	31.5	1.0	10.9	2.1	0.3	0.2
IC443	100	16.8 ± 0.9	30.9	1.0	26.1	1.4	0.4	0.2
IC443	143	11.4 ± 0.9	30.5	1.0	62.3	1.3	0.7	0.2
IC443	217	56.2 ± 4.0	30.2	1.0	234.8	5.5	2.0	0.8
IC443	353	230.3 ± 16.2	30.2	1.0	995.4	35.7	13.8	5.1
IC443	545	728.8 ± 51.4	30.2	1.0	3138.8	33.3	13.0	5.1
IC443	857	2003.5 ± 144.2	30.2	1.0	8697.4	92.1	36.0	15.6
PuppisA	30	31.5 ± 1.7	51.4	1.0	28.6	5.9	1.5	0.7
PuppisA	44	20.6 ± 1.2	49.3	1.0	22.3	2.2	0.6	0.3
PuppisA	70	13.3 ± 1.0	46.0	1.0	30.3	1.2	0.4	0.2
PuppisA	100	11.7 ± 1.1	45.6	1.0	71.6	1.3	0.5	0.2
Vela	30	470.6 ± 23.7	192.8	1.0	407.9	8.3	1.5	4.7
Vela	44	313.6 ± 15.9	192.3	1.0	323.7	3.0	0.6	2.2
Vela	70	235.4 ± 12.4	191.5	1.0	455.0	1.8	0.4	1.5
PKS1209	30	9.7 ± 0.5	71.9	1.0	12.9	1.7	0.3	0.1
PKS1209	44	8.2 ± 0.6	70.5	1.0	12.5	0.8	0.2	0.1
PKS1209	70	7.4 ± 0.9	68.2	1.0	24.3	0.6	0.1	0.1
PKS1209	100	9.7 ± 0.8	67.9	1.0	45.4	0.5	0.2	0.1
RCW86	30	3.7 ± 0.9	40.1	1.4	29.6	2.8	1.9	0.9
RCW86	44	4.0 ± 0.6	37.4	1.4	15.2	1.1	0.5	0.3
RCW86	70	2.0 ± 0.5	33.0	1.0	7.6	0.5	0.2	0.1
MSH15-56	30	55.5 ± 3.5	37.7	1.4	34.8	14.6	2.5	6.5
MSH15-56	44	38.7 ± 2.5	35.0	1.4	19.8	6.1	0.8	1.9
MSH15-56	70	22.7 ± 1.6	30.1	1.0	11.7	4.1	0.4	0.5
MSH15-56	100	18.4 ± 1.7	29.5	1.0	26.6	2.7	0.5	0.6
MSH15-56	143	12.8 ± 2.7	29.0	1.0	76.1	2.1	0.9	0.7
SN1006	30	3.6 ± 0.2	33.4	1.4	3.0	1.2	0.3	0.1
SN1006	44	3.3 ± 0.3	30.3	1.4	1.2	0.6	0.1	0.1
SN1006	70	2.6 ± 0.3	24.5	1.0	1.0	0.5	0.0	0.1
SN1006	100	2.7 ± 0.2	23.7	1.0	1.4	0.4	0.0	0.1

Notes. [a] Units for the intensities are mK for frequencies 30–353 GHz, and MJy sr^{-1} for frequencies 545–857 GHz.

[26] Department of Physics, University of California, Santa Barbara, California, U.S.A.

[27] Dipartimento di Fisica e Astronomia G. Galilei, Università degli Studi di Padova, via Marzolo 8, 35131 Padova, Italy

[28] Dipartimento di Fisica e Scienze della Terra, Università di Ferrara, Via Saragat 1, 44122 Ferrara, Italy

[29] Dipartimento di Fisica, Università La Sapienza, P. le A. Moro 2, Roma, Italy

[30] Dipartimento di Fisica, Università degli Studi di Milano, Via Celoria, 16, Milano, Italy

[31] Dipartimento di Fisica, Università degli Studi di Trieste, via A. Valerio 2, Trieste, Italy

[32] Dipartimento di Fisica, Università di Roma Tor Vergata, Via della Ricerca Scientifica, 1, Roma, Italy

[33] Discovery Center, Niels Bohr Institute, Blegdamsvej 17, Copenhagen, Denmark

[34] Discovery Center, Niels Bohr Institute, Copenhagen University, Blegdamsvej 17, Copenhagen, Denmark

[35] European Southern Observatory, ESO Vitacura, Alonso de Cordova 3107, Vitacura, Casilla 19001, Santiago, Chile

[36] European Space Agency, ESAC, Planck Science Office, Camino bajo del Castillo, s/n, Urbanización Villafranca del Castillo, Villanueva de la Cañada, Madrid, Spain

[37] European Space Agency, ESTEC, Keplerlaan 1, 2201 AZ Noordwijk, The Netherlands

[38] Facoltà di Ingegneria, Università degli Studi e-Campus, Via Isimbardi 10, Novedrate (CO), 22060, Italy

[39] Gran Sasso Science Institute, INFN, viale F. Crispi 7, 67100 L'Aquila, Italy

[40] Helsinki Institute of Physics, Gustaf Hällströmin katu 2, University of Helsinki, Helsinki, Finland

[41] INAF - Osservatorio Astrofisico di Catania, Via S. Sofia 78, Catania, Italy

[42] INAF - Osservatorio Astronomico di Padova, Vicolo dell'Osservatorio 5, Padova, Italy

[43] INAF - Osservatorio Astronomico di Roma, via di Frascati 33, Monte Porzio Catone, Italy

[44] INAF - Osservatorio Astronomico di Trieste, Via G.B. Tiepolo 11, Trieste, Italy

[45] INAF/IASF Bologna, Via Gobetti 101, Bologna, Italy

[46] INAF/IASF Milano, Via E. Bassini 15, Milano, Italy

[47] INFN, Sezione di Bologna, Via Irnerio 46, I-40126, Bologna, Italy

[48] INFN, Sezione di Roma 1, Università di Roma Sapienza, Piazzale Aldo Moro 2, 00185, Roma, Italy

[49] INFN/National Institute for Nuclear Physics, Via Valerio 2, I-34127 Trieste, Italy

[50] IPAG: Institut de Planétologie et d'Astrophysique de Grenoble, Université Grenoble Alpes, IPAG, F-38000 Grenoble, France, CNRS, IPAG, F-38000 Grenoble, France

[51] Imperial College London, Astrophysics group, Blackett Laboratory, Prince Consort Road, London, SW7 2AZ, U.K.

[52] Infrared Processing and Analysis Center, California Institute of Technology, Pasadena, CA 91125, U.S.A.

[53] Institut d'Astrophysique Spatiale, CNRS (UMR8617) Université Paris-Sud 11, Bâtiment 121, Orsay, France

[54] Institut d'Astrophysique de Paris, CNRS (UMR7095), 98 bis Boulevard Arago, F-75014, Paris, France

[55] Institute for Space Sciences, Bucharest-Magurale, Romania

[56] Institute of Astronomy, University of Cambridge, Madingley Road, Cambridge CB3 0HA, U.K.

[57] Institute of Theoretical Astrophysics, University of Oslo, Blindern, Oslo, Norway

[58] Instituto de Física de Cantabria (CSIC-Universidad de Cantabria), Avda. de los Castros s/n, Santander, Spain

[59] Istituto Nazionale di Fisica Nucleare, Sezione di Padova, via Marzolo 8, I-35131 Padova, Italy

[60] Jet Propulsion Laboratory, California Institute of Technology, 4800 Oak Grove Drive, Pasadena, California, U.S.A.

[61] Jodrell Bank Centre for Astrophysics, Alan Turing Building, School of Physics and Astronomy, The University of Manchester, Oxford Road, Manchester, M13 9PL, U.K.

[62] Kavli Institute for Cosmology Cambridge, Madingley Road, Cambridge, CB3 0HA, U.K.

[63] Kazan Federal University, 18 Kremlyovskaya St., Kazan, 420008, Russia

[64] LAL, Université Paris-Sud, CNRS/IN2P3, Orsay, France

[65] LERMA, CNRS, Observatoire de Paris, 61 Avenue de l'Observatoire, Paris, France

[66] Laboratoire AIM, IRFU/Service d'Astrophysique - CEA/DSM - CNRS - Université Paris Diderot, Bât. 709, CEA-Saclay, F-91191 Gif-sur-Yvette Cedex, France

[67] Laboratoire Traitement et Communication de l'Information, CNRS (UMR 5141) and Télécom ParisTech, 46 rue Barrault F-75634 Paris Cedex 13, France

[68] Laboratoire de Physique Subatomique et Cosmologie, Université Grenoble-Alpes, CNRS/IN2P3, 53, rue des Martyrs, 38026 Grenoble Cedex, France

[69] Laboratoire de Physique Théorique, Université Paris-Sud 11 & CNRS, Bâtiment 210, 91405 Orsay, France

[70] Lawrence Berkeley National Laboratory, Berkeley, California, U.S.A.

[71] Lebedev Physical Institute of the Russian Academy of Sciences, Astro Space Centre, 84/32 Profsoyuznaya st., Moscow, GSP-7, 117997, Russia

[72] Max-Planck-Institut für Astrophysik, Karl-Schwarzschild-Str. 1, 85741 Garching, Germany

[73] Max-Planck-Institut für Radioastronomie, Auf dem Hügel 69, 53121 Bonn, Germany

[74] National Radio Astronomy Observatory, 520 Edgemont Road, Charlottesville VA 22903-2475, U.S.A.

[75] National University of Ireland, Department of Experimental Physics, Maynooth, Co. Kildare, Ireland

[76] Nicolaus Copernicus Astronomical Center, Bartycka 18, 00-716 Warsaw, Poland

[77] Niels Bohr Institute, Blegdamsvej 17, Copenhagen, Denmark

[78] Niels Bohr Institute, Copenhagen University, Blegdamsvej 17, Copenhagen, Denmark

[79] Optical Science Laboratory, University College London, Gower Street, London, U.K.

[80] SETI Institute and SOFIA Science Center, NASA Ames Research Center, MS 211-3, Mountain View, CA 94035, U.S.A.

[81] SISSA, Astrophysics Sector, via Bonomea 265, 34136, Trieste, Italy

[82] School of Physics and Astronomy, Cardiff University, Queens Buildings, The Parade, Cardiff, CF24 3AA, U.K.

[83] Sorbonne Université-UPMC, UMR7095, Institut d'Astrophysique de Paris, 98 bis Boulevard Arago, F-75014, Paris, France

[84] Space Sciences Laboratory, University of California, Berkeley, California, U.S.A.

[85] Special Astrophysical Observatory, Russian Academy of Sciences, Nizhnij Arkhyz, Zelenchukskiy region, Karachai-Cherkessian Republic, 369167, Russia

[86] UPMC Univ Paris 06, UMR7095, 98 bis Boulevard Arago, F-75014, Paris, France

[87] Université de Toulouse, UPS-OMP, IRAP, F-31028 Toulouse cedex 4, France

[88] Universities Space Research Association, Stratospheric Observatory for Infrared Astronomy, MS 232-11, Moffett Field, CA 94035, U.S.A.

[89] University of Granada, Departamento de Física Teórica y del Cosmos, Facultad de Ciencias, Granada, Spain

[90] University of Granada, Instituto Carlos I de Física Teórica y Computacional, Granada, Spain

[91] Warsaw University Observatory, Aleje Ujazdowskie 4, 00-478 Warszawa, Poland